Probing Antiferromagnetic Hysteresis on Programmable Quantum Annealers

Elijah Pelofske,[1, *] Pratik Sathe,[2, 3] Cristiano Nisoli,[2, 4, 3] and Frank Barrows[2, 4]

[1]*Information Systems & Modeling, Los Alamos National Laboratory*
[2]*Theoretical Division, Quantum & Condensed Matter Physics, Los Alamos National Laboratory*
[3]*Information Science and Technology Institute, Los Alamos National Laboratory*
[4]*Center for Nonlinear Studies, Los Alamos National Laboratory*

Using programmable analog quantum annealing processors, we implement a sampling-based magnetic hysteresis protocol to probe the counterintuitive notion of magnetic memory of antiferromagnets. A key component of this protocol responsible for the hysteresis is a transverse field, which enables state transitions, while the magnetic field sweep is done via a longitudinal control field. We present evidence of full saturation and reversal of the hysteresis curve, as well as emergent magnetic domain mediated by quantum fluctuations that give rise to the magnetic memory effect in antiferromagnets.

I. INTRODUCTION

Quantum annealing, a type of analog quantum computation based on the quantum adiabatic theorem, aims to obtain low energy solutions for combinatorial optimization problems, or more generally from a rich manifold of metastability [1–4]. More recently, quantum annealers have been increasingly used as programmable laboratories for physical phenomenon which are otherwise inaccessible using either bulk material observables in magnetic laboratories, or classical simulation techniques [5–15].

Recently, we have expanded the phenomenological range of these experiments by introducing the first protocol to perform magnetic hysteresis measurements on D-Wave's quantum annealers, which are conceptually identical to measurements performed in a laboratory [16]. Previously, we have applied this method to ferromagnetic and $\pm J$ disordered Ising models [16, 17]. In this study, we apply our method to simulations of a counterintuitive type: hysteresis in antiferromagnetically interacting spins. We perform these experiments on four different D-Wave quantum annealing QPUs. We find several notable phenomena, including non-monotonicities similar to what has been observed in low-dimensional ferromagnetic models [17]. Where meaningful, we extract both spin structure factor and the antiferromagnetic (Néel) order parameter from the $2D$ antiferromagnetic models to probe the magnetic order throughout the hysteresis cycles.

Historically, the primary type of magnetic material which clearly exhibits magnetic hysteresis are ferromagnetic compounds. The hysteresis in ferromagnetism comes from the breakdown of ergodicity associated with the spontaneous symmetry breaking around a specific magnetization. While a sufficiently strong field can polarize an antiferromagnet, one would not easily expect hysteretic magnetization, because the local field acts to destroy the net moment.

Antiferromagnetic hysteresis is a rare but known phenomenon explained with diverse mechanisms in various systems [18–23], though typically not in *purely* antiferromagnetic models, where it remains poorly understood. Indeed, even the text-book explanation for standard, ferromagnetic hysteresis in terms of sticky metastabilities alone, proves deceptively simple: glossing over, in the classical case, the effects of kinetics in dynamical hysteresis [24, 25]; and neglecting, in quantum systems, the role of quantum fluctuations in driving state transitions via tunneling. This motivates a study of hysteresis precisely where such metastability is absent [25]: the pure antiferromagnet.

This work explores exotic hysteresis in systems of antiferromagnetic interacting qubits exposed to controlled quantum fluctuations, providing a proof of principle of magnetic memory. We expand the scope of frustrated quantum magnet [26] studies to include out of equilibrium antiferromagnetic memory protocols, which are programmable via D-Wave quantum annealing processor. Because magnetic hysteresis is a fundamental emergent phenomenon of interacting magnetic spins, the possibility of analog quantum experiments of antiferromagnetic hysteresis are a notable computational capability of contemporary, noisy, quantum annealing processors.

II. METHODS

A. The Hysteresis Protocol

We perform our experiments, often called analog simulations, on programmable quantum annealers manufactured by D-Wave Systems [27, 28]. These devices use superconducting flux qubits [29–32], connected in a graph comprising repeating tileable subgraph units. The full Hamiltonian that D-Wave hardware implements is

$$\mathcal{H} = -\frac{A(s)}{2} \sum_i \hat{\sigma}_x^{(i)} + \frac{B(s)}{2} \left[g(t) \sum_i h_i \hat{\sigma}_z^{(i)} + \sum_{i \neq j} J_{ij} \hat{\sigma}_z^{(i)} \hat{\sigma}_z^{(j)} \right], \tag{1}$$

where s is an annealing parameter that can be controlled in time, and $A(s)$ and $B(s)$ are hardware-dependent energy scales that multiply the transverse and longitudinal components of the Hamiltonian respectively. The latter is defined by programmable, unitless coupler interactions J_{ij} and site-dependent longitudinal fields h_i. The σ_x Pauli term is the driving Hamiltonian which facilitates state transitions in the quantum annealer because it does not commute with the classical Hamiltonian defined by the J_{ij} and h_i terms. Crucially, $g(t)$ is a global time-dependent multiplier on all of the individual fields h_i, which can be controlled independently of s, and is thus central to our methods, as described in ref. [16]. In the QPU programming, each h_i is set to the maximum allowed normalized-hardware programmable value of 4.

Appendix A plots the hardware-specific functions $A(s)$ and $B(s)$. Importantly, our measurements are on open quantum systems [33, 34] in a quasistatic annealing time regime [35]. Various sources of error are present in the D-Wave quantum annealing processor computations including coupling to the environment, analog control errors, spurious qubit couplings, and device characteristic drift over time [36–43].

We apply the magnetic hysteresis protocol outlined in Ref. [16], with a small modification— the inclusion of calibration refinement of flux bias offsets outlined in ref. [44] for the whole-lattice experiments. Otherwise, all other analog hardware parameters remain the same as in ref. [16], in particular for all measurements we use an 11.2 microsecond total (final) "annealing time", because what we perform is, in fact, a modified "forward-anneal" with a pause in the annealing parameter s during which we activate the longitudinal field. This hysteresis protocol is a probabilistic, sampling based protocol, and it requires both the transverse field on the D-Wave QPUs, which facilitates state transitions, as well as a sufficiently strong lattice coupling J, without which no hysteresis can be recorded, and most importantly a time-varying longitudinal field which drives the magnetization ramping and reversal (the "h-gain" hardware control). As in Ref. [16], we report *average* magnetization as a function of applied longitudinal field. Note that we flip the sign of the magnetization to compensate for the sign of the D-Wave QPU Hamiltonian Eq. (1).

The protocol has several important tunable parameters. One is, the fixed ratio of Γ/J at which the hysteresis cycle is swept: without sufficient transverse field, the state does not change (not even due to thermal fluctuations), and if the transverse field is too strong then we are left with featureless unpolarized states with memoryless trajectories. Additionally, the longitudinal field must be sufficiently strong to force the system to become fully po-
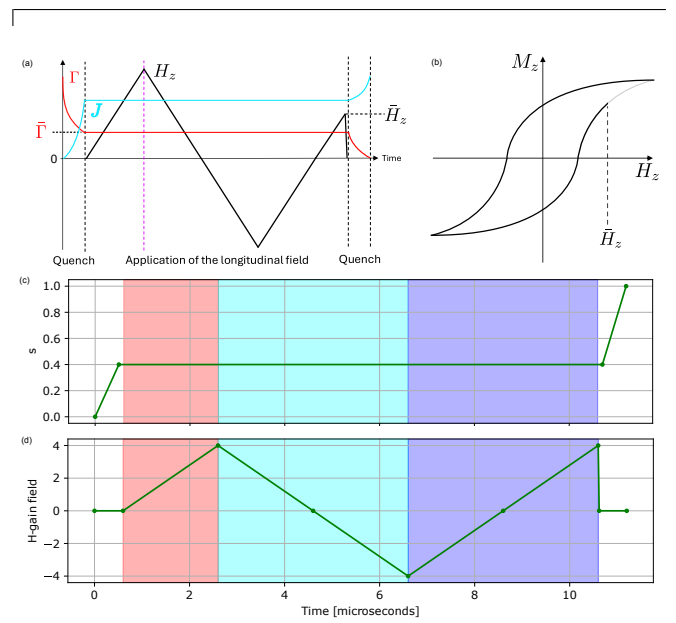

FIG. 1: **Schematic of the magnetic hysteresis protocol**. Panel a shows the field ramps over time, as schematics (not actual energy scales or timescales) where we begin recording magnetization at the maximum-polarization longitudinal field denoted by the dashed purple vertical line, and panel b shows the conceptual tracing of the average magnetization response to the applied longitudinal field H_z. Panels c and d show the programmed D-Wave hardware waveforms for the *final* simulation time of $11.2\mu s$, where s is the "anneal-schedule" control parameter, and the h-gain field is H_z. Adapted from ref. [16].

larized against the antiferromagnetic bonds: therefore if the D-Wave hardware controls do not allow significantly strong longitudinal fields, only minor hysteresis loops are obtained. In principle one could always obtain saturation by using smaller coupling values, but that would amplify the role of thermal fluctuations and further destroy memory in an undesirable manner. Each QPU also has a different maximum longitudinal field that can be applied; the maximum field values of the h-gain schedule, i.e., of $g(t)$ in Eq. (1) are provided in Table I.

B. Antiferromagnetic Ising Models and Embeddings

We consider three different types of uniformly weighted antiferromagnetic Ising models: 1-dimensional with periodic boundary conditions (an Ising model on a ring), 2-dimensional with open boundary conditions, and a specific type of "pseudo-3-dimensional" model that involves the full hardware graph.

D-Wave QPU Chip	Graph name	Qubits	Couplers	Maximum h-gain field strength
`Advantage_system4.1`	Pegasus P_{16}	5627	40279	± 1.75
`Advantage_system6.4`	Pegasus P_{16}	5612	40088	± 4
`Advantage_system7.1`	Pegasus P_{16}	5554	39238	± 3.5
`Advantage2_prototype2.6`	Zephyr $Z_{6,4}$	1248	10827	± 3

TABLE I: D-Wave QPU summary, where the maximum possible h-gain field that can be applied is in hardware-normalized units (relative to the specific Hamiltonian on each QPU).

The 2D antiferromagnetic case corresponds to entirely unfrustrated magnetic systems (for even L_x and L_y) whose ground state is ordered with an antiferromagnetic order parameter equal to one below the critical temperature. The (antiferromagnetic) "pseudo-3D" hardware lattice is magnetically frustrated; it is not bipartite. The 1D antiferromagnetic systems all have an odd number of spins, so they are slightly frustrated – on one edge, in their ground-state.

For the 1-dimensional rings with periodic boundary conditions we embed the largest rings that we can using a reasonable amount of compute time employing the subgraph isomorphism finder called the Glasgow solver [45], which is part of the `minorminer` package [46]. The embedded 1D spin system sizes are: 4905 qubits on `Advantage_system4.1`; 4885 qubits on `Advantage_system6.4`, 4791 qubits on `Advantage_system7.1`; and 1131 qubits on `Advantage2_prototype2.6`.

Similarly, the 2-dimensional square grids with open boundary conditions are embedded using the Glasgow subgraph isomorphism finder [45], for the largest grids that we can find a native embedding for in a fixed reasonable amount of CPU compute time. For `Advantage_system4.1` this is a 32×32 grid, for `Advantage_system6.4` this is a 32×32 grid, for `Advantage_system7.1` this is 33×33, and for `Advantage2_prototype2.6` this is 26×26.

For all of these Ising models we use a direct qubit to spin embedding, meaning that no minor embedding is used, thus avoiding several types of issues for this type of sampling-based non-equilibrium magnetic simulation protocol [47].

In the hardware-defined antiferromagnets we set every single edge on the hardware graph that can be programmed, to an antiferromagnetic weight. Therefore, these models have the same number of spins as the number of qubits on each QPU and the same number of edges as the number of couplers on each QPU, as summarized in Table I. The QPUs have either Pegasus [48, 49] or Zephyr [50] connectivity. All four of the D-Wave QPUs used in this study typically physically operate at approximately 15 mK.

All of the antiferromagnetic models are programmed with the maximum coupler strength that can be specified on the hardware, which is $J = +1$ on all couplers (in hardware normalized programmable units, see Appendix A).

C.   Statistic Balancing Calibration Refinement

During experiments on D-Wave QPUs, in particular on the models defined on the entire hardware graph, we noticed that on some of the QPUs the results were very noisy. This noise can come from non-idealities in quantum annealer, including small fluctuations in the magnetic environment. To reduce the impact of these effects, we implement an observable balancing calibration refinement technique described in Ref. [44]. This general technique of statistic balancing is a form of calibration refinement typically referred to as "shimming", and has been used in numerous previous studies on D-Wave quantum annealers [10, 12, 15, 33, 44, 51–55]. This calibration procedure can in principle be applied to any programmed Ising model on analog hardware, but it has been especially useful for exploring sensitive phenomena, such as quantum quench dynamics and fluctuations near thermodynamic phase transitions. In this study, we balance the distribution of magnetization at each qubit, since in an ideal experiment (in the absence of a longitudinal field) we expect the mean magnetization of each qubit to equal 0. To that end, we iteratively modify the flux bias offsets (FBOs) of each qubit separately, achieving a lower spread of qubit magnetization with each iteration. The FBO update rules applied to each qubit are uniform across the entire lattice, i.e., the bulk and edge qubits are treated identically, unlike in some prior studies [15]. More details are described in Appendix B.

More advanced statistic balancing could be used in order to refine the analog experiments for even higher precision simulations, in the form of balancing the antiferromagnetic couplers, as well as the statistics resulting from the uniformly applied longitudinal fields h_i, both of which would require substantial QPU time usage. Ideally, calibration of these local fields would be (independently) performed for every applied h-gain field strength during the slicing of the h-gain sweep, which would involve a significant amount of QPU time to perform, even for a single hysteresis cycle. We leave these more complex balancing techniques to future study, and for the present simulations we focus on balancing single-site magnetization using flux bias offsets, which results in more stable hysteresis cycle measurements. We report both calibrated and uncalibrated data on the D-Wave hardware graph defined antiferromagnets.

D. Observables

The main observable is the average longitudinal magnetization, defined as the normalized sum of all the spins σ_i^z read in the z direction

$$M^z = \frac{1}{N} \sum_i \langle \sigma_i^z \rangle, \qquad (2)$$

where $\langle \ldots \rangle$ denotes an average over 2,000 samples (8,000 samples in the case of the full hardware graphs) measured on the hardware sampler. The experimental average over a relatively large number of samples mitigates the possibility of apparent ordering due to finite sampling effects, which may occur if the number of samples is especially small.

Our access to the individual degrees of freedom allows for the direct extraction of other interesting observables, including the real space maps of spin configurations, which we will show in section III. A useful and frequent observable in experiments in magnetism is the magnetic structure factor, which gives clear visual evidence for different type of magnetic ordering during hysteresis cycles. While in experiments it is obtained by neutron scattering, we can reconstruct it from individual spins, as

$$S(\mathbf{q}) = \langle \sum_{i,j} e^{i\mathbf{q}\cdot(\mathbf{r}_i-\mathbf{r}_j)} \sigma_z^i \sigma_z^j \rangle \qquad (3)$$

where $\mathbf{r}$ denotes spin lattice locations. For the 2D case on a square lattice, we discretize the momentum vector $\mathbf{q}$ on a 200×200 uniformly spaced grid spanning $(-2\pi, 2\pi)$ along both dimensions for individual spin configurations. The computation of the structure factors is greatly accelerated by the Python libraries Numba and Numpy [56, 57].

We do not employ the magnetic structure factor for the "pseudo-3D" full hardware graphs case as in absence of an sensible definition for a Brillouin zone there is no obvious way to define a version whose plots would be informative.

While the structure factor provides information the ordering of spins, it is agnostic of a notion of order properly intended as a spontaneous symmetry breaking (here Z_2 symmetry. A natural quantity to examine in these hysteresis simulations is the *antiferromagnetic order parameter*, also known as the Néel order parameter. This quantifies whether there is long range antiferromagnetic ordering, and is a natural quantity to examine in these out-of-equilibrium driving hysteresis simulations on antiferromagnetic systems. Unlike magnetization, the *staggered* antiferromagnetic order parameter is inaccessible to experiments in a magnetic laboratory, but accessible to experiments on quantum annealers because they provide information on the elementary degree of freedom. We denote it as M_s for "staggered" magnetization, and

is defined as

$$M_s = \frac{1}{N} \sum_i (-1)^i \langle \sigma_i^z \rangle, \qquad (4)$$

where $(-1)^i$ denotes alternating staggered sign-flips between the two bi-partitions of the lattice: the 2D systems are bipartite graphs. For the 2D systems it forms a staggered checkerboard pattern. $\langle S_i \rangle$ is the average measured magnetization of qubit i, and N is the total number of spins in the system. In the case of the 1D and the 3D antiferromagnetic models, the graphs are not bipartite and their ground-states are frustrated; in the case of the 1D models there is a single domain wall somewhere on the ring in the ground-state, because they have an odd number of spins. For the D-Wave hardware defined graphs a staggered order parameter cannot be defined in any obvious way, and a similar issue arises for the odd length 1D models we consider in this study due to their periodic boundary conditions. Therefore, we report the Néel order parameter only for the open boundary condition 2D models. For the 1D models, we examine domain wall density, which is a natural measure to examine because the ground-state configuration has a minimum number of domain walls of 1, and then when the model becomes fully saturated in the hysteresis cycle (if the longitudinal field is sufficiently strong) the proportion of domain walls is maximized.

III. RESULTS

We report antiferromagnetic hysteresis in 1D systems, in section III A, in 2D antiferromagnetic systems in section III B, and lastly in 3D (specifically whole-hardware graph defined) antiferromagnetic models in section III D.

A. 1-Dimensional Antiferromagnet Experiments

Figure 2 presents magnetic hysteresis simulations on 1D antiferromagnets, with periodic boundary conditions, performed at different values of s and thus of Γ/J. This shows interesting non-monotonic features, in particular a "pinch-point" which occurs at $s = 0.6$. Moreover, when Γ/J is sufficiently small, we achieve full polarization of the antiferromagnetic model, which is elusive for larger values of Γ.

Figure 3 shows examples of 1D real-space spin configurations sampled during one of the hysteresis cycles run on the D-Wave QPU `Advantage2_system2.6`, specifically in the non-saturated regions of the cycle. These spin configurations show very small antiferromagnetic domains at small M_z; the distribution of alternating sign spins is not uniform – which could be in part due to small J coupling energy scales differences on the analog hardware. One sees formation of magnetic domains for larger M_z, as expected.
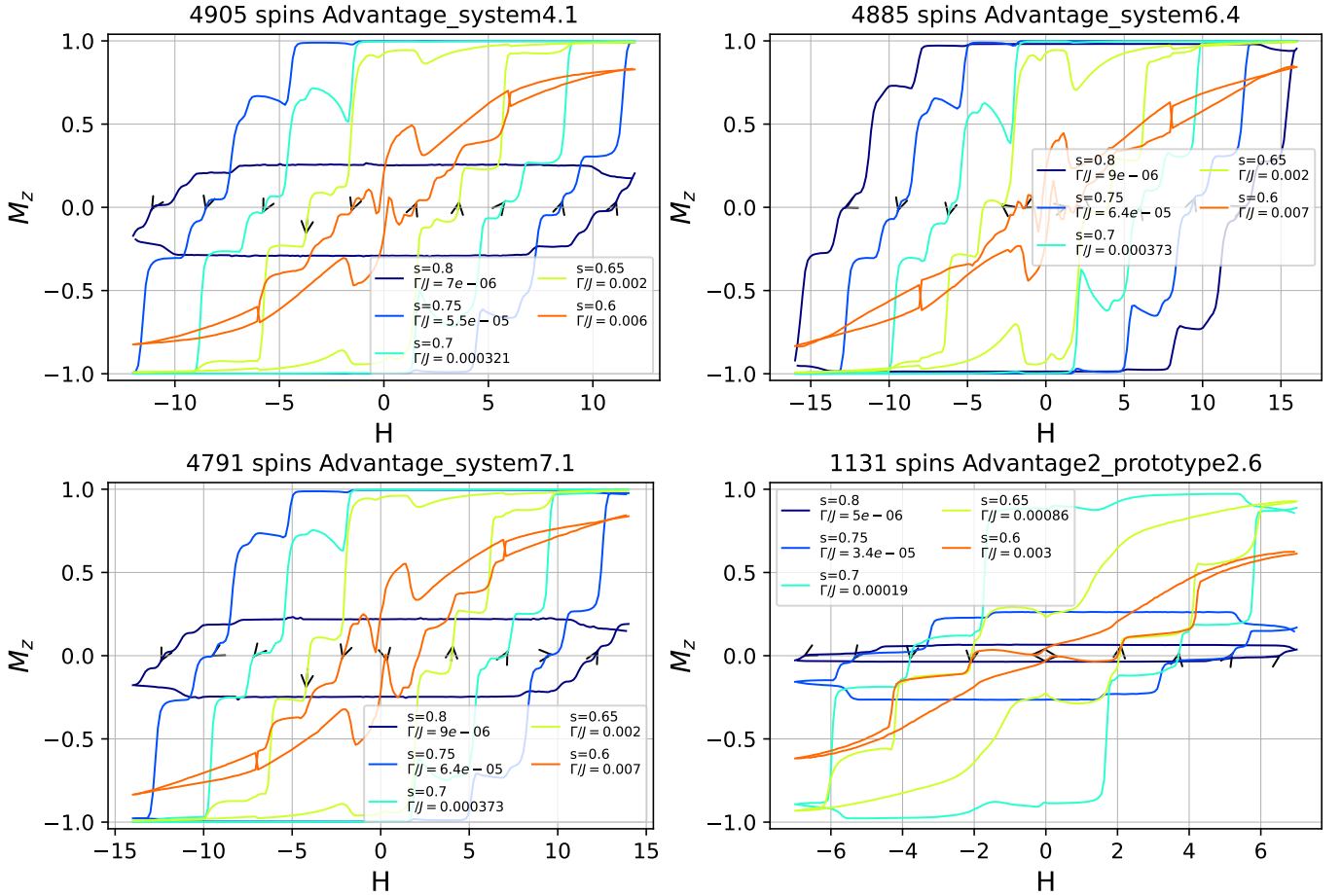
FIG. 2: Magnetic hysteresis on 1D odd antiferromagnetic rings. Average magnetization (y-axis) as a function of the applied longitudinal field H (x-axis). The overlaid black arrows on the average magnetization lines sampled from the QPUs simultaneously denote the time-progression of the experiment, as well as the direction of the longitudinal field sweeps. The H field units are in normalized hardware programmable units, see Appendix A. The different lines correspond to D-Wave experiments performed at different anneal-schedule-pauses, defined by s, which corresponds to a particular physical field ratio of Γ/J (denoted in the legend).
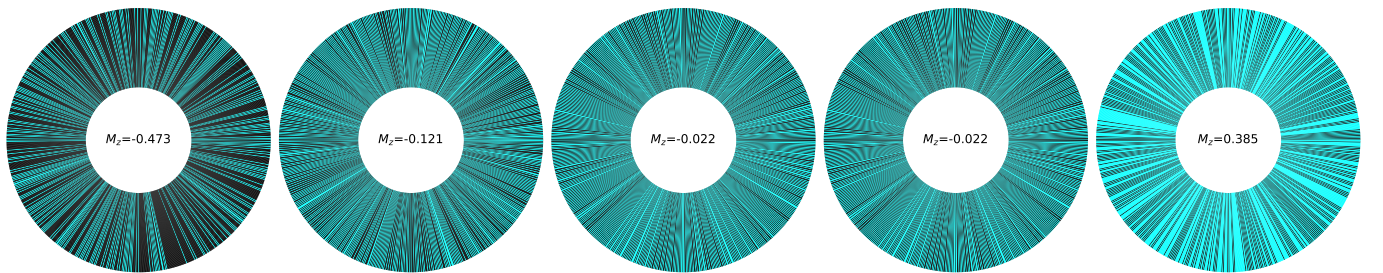
FIG. 3: Selected example 1D antiferromagnet spin configurations measured during the hysteresis cycle run on `Advantage2_prototype2.6` (at $s = 0.7$), comprised of 1131 spins. Each spin configuration is from a different applied longitudinal field value in the non-saturated region of the hysteresis cycle. The spin configurations are shown as a circular annular wedge plot where black slice denote spin down qubit measurements and cyan slices denote spin up qubit measurements. The net magnetization for each sample is shown in the center of each plot.

Figure 4 reports 1D domain wall density in the 1D hysteresis cycles, including the proportion of ↓↓ domain walls (note that, like magnetization, the sign of this domain wall has been reversed in order to compensate for the sign of the D-Wave processor Hamiltonian [16]).
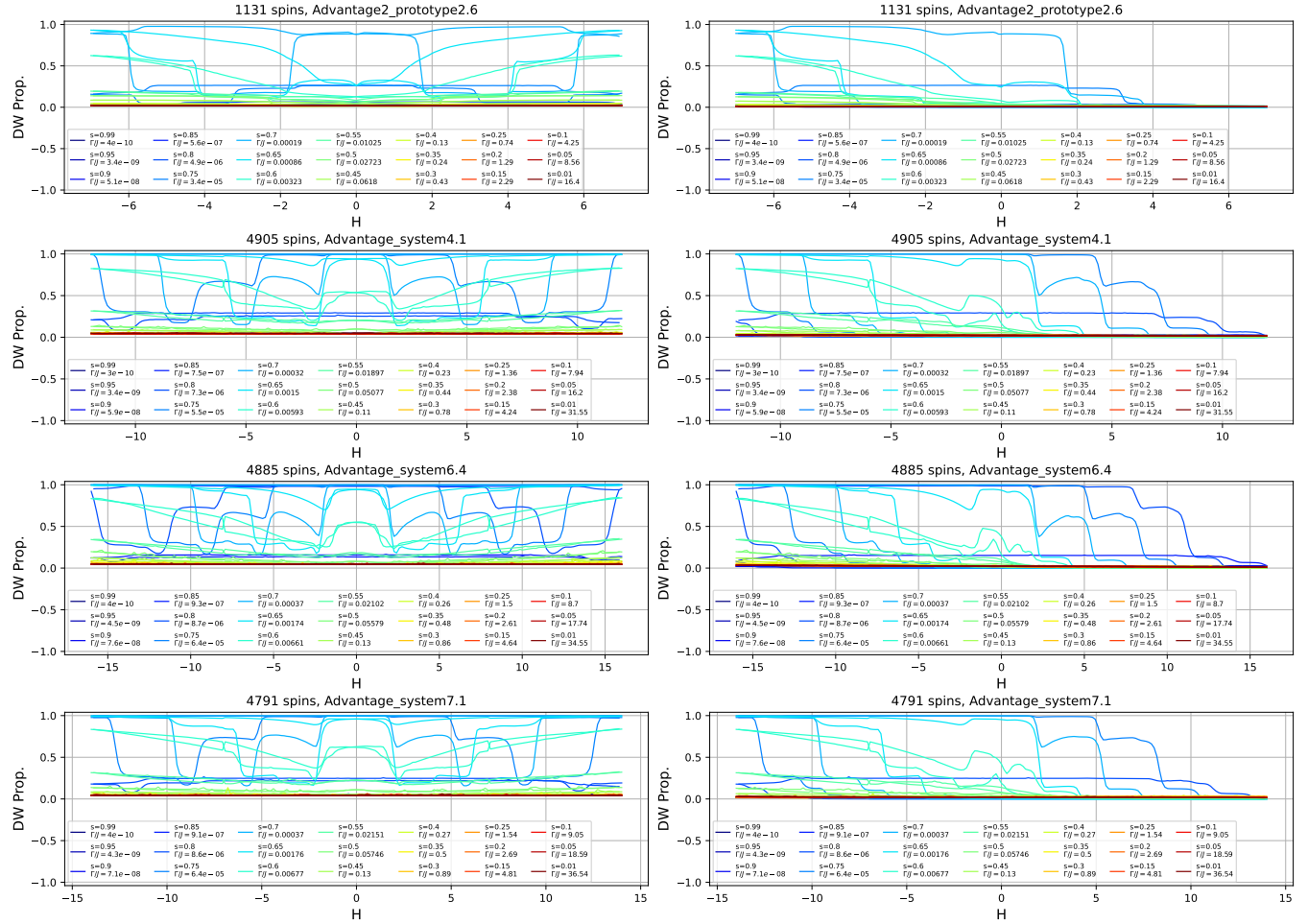
FIG. 4: Domain wall density (y-axis) on the 1D antiferromagnetic rings during the hysteresis cycles as a function of applied longitudinal field H. Left hand column shows the total, average, domain wall wall density, regardless of the sign of the domain wall. Right hand column shows the spin down ($\downarrow\downarrow$) domain wall density. Like in the prior hysteresis result plots, each line that is plotted corresponds to a paused Γ/J value on the D-Wave processor. Each row corresponds to the different system size embedded on a different quantum annealing processor. Note that because these rings have an odd number of spins, we are always guaranteed to have at least one pinned domain wall somewhere on the ring.

1. Odd Rings, Domain-Wall Sectors, and Their Use as a Defect Transport Probe

To provide more insight on these experiments, consider the transverse-field Ising antiferromagnet on a ring,

$$H = J\sum_{i=1}^{N}\sigma_i^z\sigma_{i+1}^z \; - \; h\sum_{i=1}^{N}\sigma_i^z \; - \; \Gamma\sum_{i=1}^{N}\sigma_i^x, \quad (5)$$

with $\sigma_{N+1}^z \equiv \sigma_1^z$ and $J > 0$. Because N is odd, boundary conditions enforce an odd number D of antiferromagnetic bonds, i.e., there is always at least one domain wall, and specifically the ground-state configuration has exactly one domain wall. At small $|h|$ and $\Gamma \ll J$, the low-energy manifold contains a single domain wall, $D = 1$, whose position is N-fold degenerate.

Local spin flips generated by the transverse part of the Hamiltonian, proportional to Γ, toggle the two bonds adjacent to the flipped site, so the total number of domain walls changes by 0 or ± 2; consequently, the *parity* of D is conserved by any sequence of local flips. This parity is a robust label: an odd-N ring remains in the odd-D sector. Within that sector, the domain wall has a sign, corresponding to two spin-up or two spin-down. A longitudinal field $h \neq 0$ breaks the global $\mathbb{Z}_2$ symmetry and splits these two local configurations in energy. These are not distinct dynamical sectors once $\Gamma > 0$, because a single spin flip at the wall converts a spin-up domain wall to a spin-down domain wall (and vice-versa) while shifting the wall by one bond. Thus, odd rings naturally realize a single-wall system in which Γ drives coherent domain-wall motion and h biases its drift.

This built-in, mobile defect makes odd rings a probe of quantum-assisted defect dynamics and antiferromagnetic hysteresis. In contrast, an even-N ring possesses a wall-free Néel lowest energy configuration; reversal at small $|h|$ must first nucleate a kink–antikink pair (energy
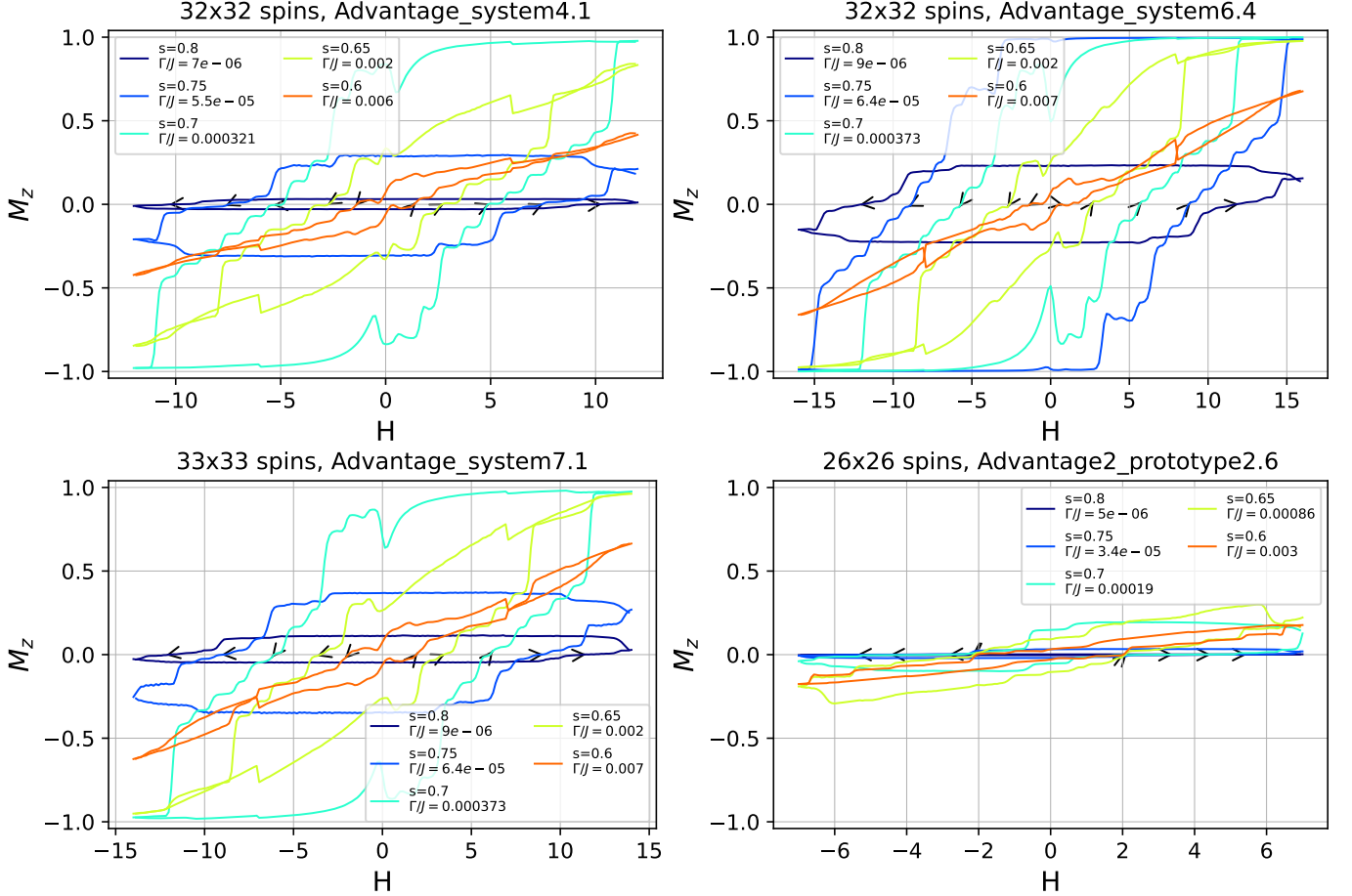
FIG. 5: Magnetic hysteresis on 2D antiferromagnetic square lattices, on four different D-Wave quantum annealers. Average magnetization (y-axis) as a function of the applied longitudinal field (x-axis). The overlaid black arrows on the average magnetization lines sampled from the QPUs simultaneously denote the time-progression of the analog simulations, as well as the direction of the longitudinal field sweeps.

cost $\approx 4J$ at $\Gamma = 0$), which strongly suppresses response and complicates interpretation. Because even rings require pair creation, their low-field loops are comparatively featureless and are not informative about defect-transport dynamics, we therefore concentrate on odd rings for quantitative analysis. For this reason, and because our experiments target quantum assisted transport and pinning phenomena, we restrict to odd rings in the all 1-dimensional experiments in this study.

Weak static inhomogeneity (bond or field offsets) pins the wall at preferred bonds. At a pinned location the two local sign states form a driven two-level subsystem; the transverse field Γ mixes them, while h sets their energy difference. As detailed below, this competition produces an avoided crossing and underlies the stick–slip dynamics and step-like magnetization changes characteristic of the antiferromagnetic hysteresis we observe.

2. Domain-wall Theory: Effective Hamiltonian, Dispersion, and Many-Wall Processes

In the single-wall regime we label basis states $|j, w\rangle$, where $j \in \{1, \ldots, N\}$ denotes the bond that hosts the domain wall and $w = \pm 1$ denotes its domain wall sign. In this subspace the exchange energy is position independent,

$$E_J = -J(N - 2), \tag{6}$$

because one bond is ferromagnetic $(+J)$ and the remaining $N - 1$ bonds are antiferromagnetic $(-J)$. The longitudinal field contributes a term that depends only on the wall sign: for odd N the total magnetization in a one-wall state is $M = \sum_i \sigma_i^z = w$, so

$$H_h \to -hw \quad \text{on} \quad |j, w\rangle. \tag{7}$$

A single σ^x acting on either spin adjacent to the wall reverses that spin, toggles the wall sign, and shifts the wall by one bond. To leading order in Γ/J this yields nearest-neighbor hopping in the $|j, w\rangle$ basis,
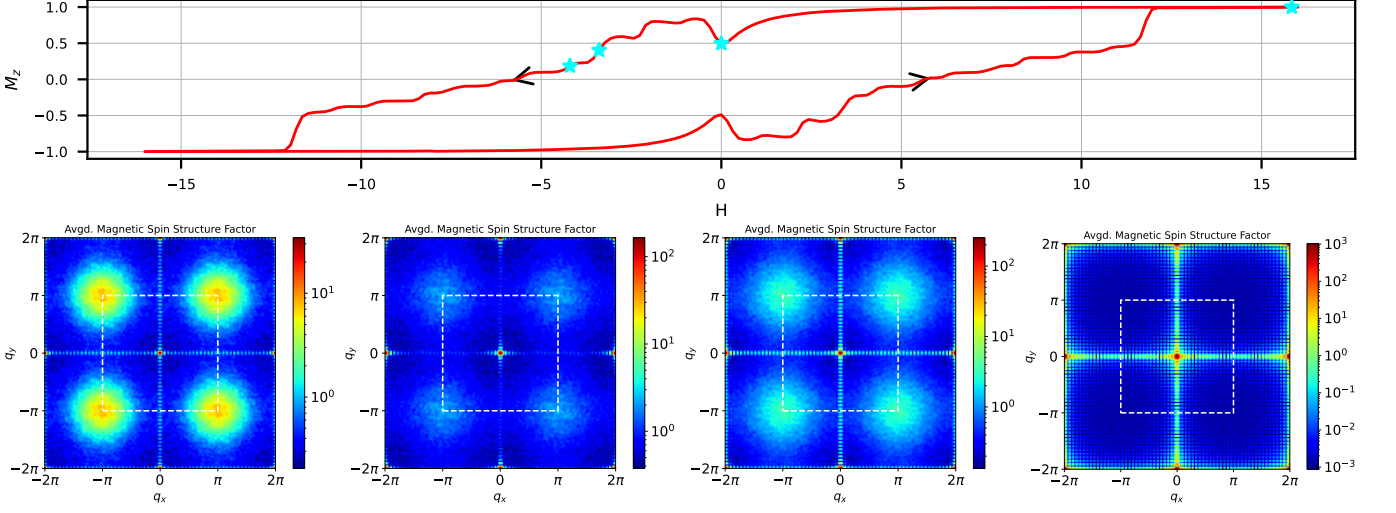
FIG. 6: Magnetic structure factors $|S(q)|$ heatmaps (bottom row) within the 2D antiferromagnetic hysteresis cycles (averaged over 100 independent samples), run on `Advantage_system6.4` at $s = 0.7$. The Ising model being simulated is a 32×32 grid of (antiferromagnetically coupled) spins, open boundary conditions. The top row shows the single hysteresis cycle in terms of M_z average magnetization, from which we extracted $|S(q)|$ heatmaps for 4 points along the first longitudinal field sweep, denoted by cyan asterisks. The dashed white line on the structure factor heat maps outlines the first Brillouin zone. The heat maps are log-scaled and scales are specific to each heatmap sub-plot. The order of the $|S(q)|$ heatmaps follows the same sweep direction denoted by the top hysteresis cycle plot (the SSF from the fully saturated regime is shown in the right hand sub-plot). Note the peaks at the corner of the Brillouin zone denoting large antiferromagnetic clusters, and coexisting with a growing peak at the center denoting magnetization.

$$H_{\text{eff}} = E_J + \sum_j \left[-hw\, |j, w\rangle \langle j, w| - \Gamma \big(|j + 1, -w\rangle \langle j, w| + |j - 1, -w\rangle \langle j, w| \big) \right], \tag{8}$$

with periodic indexing $j \equiv j+N$. Equation (8) is a tight-binding model on a two-sublattice (sign) chain.

For a homogeneous ring we diagonalize with Bloch states $|k, w\rangle = \frac{1}{\sqrt{N}} \sum_j e^{ikj} |j, w\rangle$, $k = 2\pi m/N$. In the $\{|k, +\rangle, |k, -\rangle\}$ basis the Bloch Hamiltonian reads

$$\mathcal{H}(k) = -h\sigma^z - 2\Gamma \cos(k)\, \sigma^x, \tag{9}$$

with eigenenergies

$$E_\pm(k) = E_J \pm \sqrt{h^2 + 4\Gamma^2 \cos^2(k)}. \tag{10}$$

Thus the transverse field endows the wall with a hopping amplitude $\sim \Gamma$ and, at $h \approx 0$, a single-domain-wall spectrum spanning an energy width 4Γ; the time dependent longitudinal field can populate excited one-wall states. A finite longitudinal field splits the two bands by at least $2|h|$ (at $k = \pi$), producing a drift bias for wall motion. The corresponding group velocity is

$$v_\pm(k) = \pm \frac{2\Gamma^2 \sin(k)}{\sqrt{h^2 + 4\Gamma^2 \cos^2(k)}}. \tag{11}$$

While odd N fixes the wall-number parity, additional kink–antikink pairs can be nucleated at finite drive. At $\Gamma = 0$ and small $|h|$ a single local spin flip in a Néel region

creates two additional domain walls and costs

$$\Delta E_{\text{pair}} \approx 4J - 2h\delta M, \tag{12}$$

with $\delta M = \pm 1$ in our normalization ($\sum_i \sigma_i^z = M$). Quantum mechanically, pair creation arises from higher-order virtual processes in Γ/J, while annihilation occurs when a wall meets an antiwall. On our platform thermal activation is negligible; the dynamics is therefore dominated by wall hopping, field-biased drift, quantum-assisted pair nucleation, and annihilation.

The interplay of hopping ($\sim \Gamma$) and field bias (h), pinning, and rare nucleation/annihilation events produces the antiferromagnetic hysteresis observed in odd rings. In the single-wall-dominated regime, magnetization evolves via sequences of hops punctuated by depinning events at local avoided crossings, generating discrete, Barkhausen-like steps. As the drive amplitude increases, occasional nucleation events seed additional walls which drift and annihilate; this "dilute domain-wall gas" smooths the loop while preserving a strong odd-ring response near low fields. A simple estimate gives the pair-creation energy $\Delta E_{\text{pair}} \approx 4J - 2h\delta M$, so pair nucleation becomes likely once $|h| \sim 2J$, beyond this "nucleation threshold" the loop evolves in a dilute domain-wall gas rather than by single-wall motion. In the data the rise of total domain

wall density and magnetization reversal set in around this scale.

For odd-N antiferromagnetic rings the domain-wall number D is constrained to be odd, in the regime of small $|h|$ with $\Gamma \ll J$ the the lowest-energy states have a single domain wall. In Figure 4,in the same low-field window the sign-resolved wall proportion exhibits a strong, hysteretic bias between $\uparrow\uparrow$ and $\downarrow\downarrow$ walls, with forward–reverse asymmetry. This pattern—weak change in total domain wall proportion but strong, history-dependent redistribution between the two wall signs—is exactly what the effective single-wall Hamiltonian predicts: h splits the two wall-sign states $w = \pm 1$ while Γ mixes them, yielding a biased two-level population that traces a hysteresis loop. In equilibrium this bias would reduce to a sigmoidal form $\frac{1}{2}[1 + \tanh(\beta_{\text{eff}} h)]$.

As $|h|$ grows the total domain wall proportion becomes large and the loop area is dominated by many-wall dynamics. The conspicuous non-monotonicity near $|h| \approx 1$ at $s \approx 0.6$ lies in this regime. Such large non-monotonicities can be understood as a result of synchronized depinning at reproducible nucleation fields set by hardware pinning, i.e., pinning sites and hopping barriers introduced by hardware disorder and inhomogeneities in device parameters. The non-monotonicities and resulting Barkhausen steps survive ensemble averaging because those nucleation fields recur shot-to-shot.

B. 2-Dimensional Antiferromagnet Experiments

Figure 5 presents 2-dimensional antiferromagnetic hysteresis simulations. Here once again we see full saturation can be achieved under certain Γ/J simulations. Although, on the `Advantage2_prototype2.6` processor, the maximum applied longitudinal field that can be applied is comparatively weaker than on the other devices, resulting in the net magnetization not being pushed greater than ± 0.5 under any Γ/J value, resulting in very flat antiferromagnetic hysteresis minor-loops.

Here we can also extract the spin structure factor in order to examine the types of magnetic ordering that occur during the hysteresis cycles. Figures 6, 7, 8, all show averaged magnetic structure factors from various points along the antiferromagnetic hysteresis cycles. We see clear boundary effects (due to the open boundary conditions) that occur closer to the demagnetized regions, seen as lines along $x = y = 0$ axes. In the saturated regimes, we see either bright peaks along $q_x = \pi$ and $q_y = \pi$ when Γ/J is high (meaning, the magnetization is not fully saturated), or closer to ferromagnetic ordering when the ratio Γ/J is smaller and also the longitudinal field is strong enough. But the clearest signal we see is strong antiferromagnetic ordering, with peaks at the four corners of the first Brillouin zone, as the systems become more demagnetized.

Figures 9 and 10 show examples of real space single-spin configurations measured during one of the 2-dimensional antiferromagnet hysteresis cycles. These samples show fragmentation into domain walls of the expected checkerboard ordering in the ground-state of the 2D square antiferromagnet, and moreover we see clear boundary effects (due to the open boundary conditions) as the system becomes more magnetized. To better illustrate the antiferromagnetic domains in Figs 9 and 10 we plot also on the bipartite lattice the domain height function

$$\tau_{i_x i_y} = (-1)^{i_x + i_y} \, \sigma^z_{i_x i_y}, \tag{13}$$

which is uniform and valued valued ± 1 in each domain. Domain walls are then the contours separating $\tau = +1$ and $\tau = -1$. Clearly, it is related to the antiferromagnetic order parameter via $M_s = \sum_{i_x i_y} \tau_{i_x, i_y}/N$.

In our finite 2D samples the reversal appears to proceed through a competition between nucleation of favorably oriented antiferromagnetic droplets and propagation and roughening of pre-existing interfaces, associated with antiferromagnetic symmetry breaking, as seen in in Figs 9 and 10. Open boundaries play a decisive role: edges and, in particular, corners reduce the interfacial cost, so the first irreversible events predominantly originate at the boundary. Once a supercritical droplet appears, growth continues mainly by interfacial translation (with occasional coalescence when neighboring droplets meet), producing the step-like changes in magnetization that are characteristic of pinned, driven interfaces. At larger field magnitude the rate of new-droplet formation increases and the loop correspondingly smooths as propagation competes with fresh nucleation.

These processes leave clear fingerprints in the spin-structure factor. Near saturation the structure factor weight concentrates around $\mathbf{q}=0$, reflecting the large polarized regions. As the field is swept toward the demagnetized regime, intensity migrates to antiferromagnetic wavevectors at the corners of the Brillouin zone, consistent with the build-up of checkerboard order driven by local field, inside expanding droplets and along translating interfaces. As the field swipes, the hysteresis emerges from the polarized domain walls.

Because of the finite window and open boundaries, we also observe streaks of intensity aligned with the axes of the Brillouin zone, which track the prevalence of straight boundary-pinned segments. On the return sweep, the same features recur with a field offset set by the pinning landscape, yielding a reproducible hysteretic trajectory in both the net magnetization and the structure factor.

While both reciprocal space and real space data show formation of large antiferromagnetic domains and their coexistence with net magnetization, a relevant question is whether data shows order properly intended as spontaneous antiferromagnetic symmetry breaking. To explore that, we move to the Néel order parameter [Eq. (4)]. We focus on the hysteretic region of s, and separate each hysteresis cycle by Γ/J in order to make visualization clear.
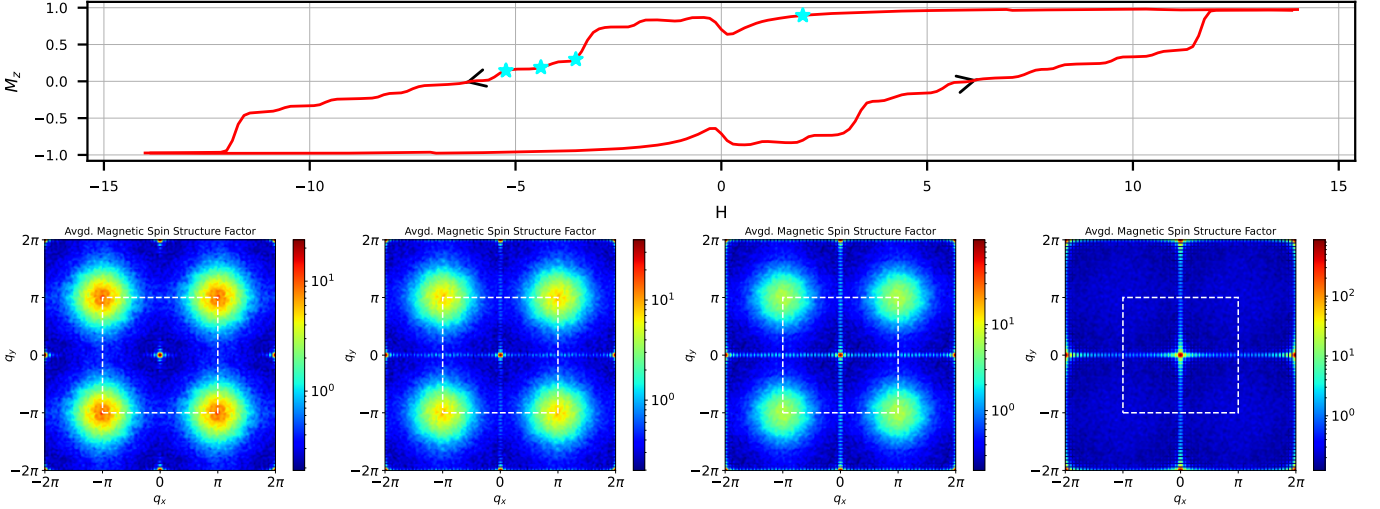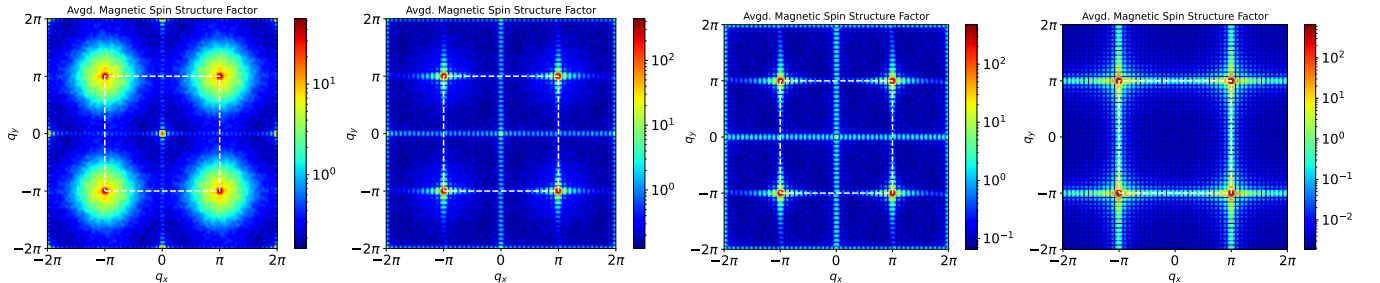
FIG. 7: Magnetic structure factors $|S(q)|$ heatmaps (bottom row) within the 2D antiferromagnetic hysteresis cycles (averaged over 100 independent samples), run on `Advantage_system7.1` at $s = 0.7$. The Ising model being simulated is a 33×33 grid of (antiferromagnetically coupled) spins, open boundary conditions. The top row shows the single hysteresis cycle in terms of M_z average magnetization, from which we extracted $|S(q)|$ heatmaps for 4 points along the first longitudinal field sweep, denoted by cyan asterisks. The dashed white line on the structure factor heat maps outlines the first Brillouin zone. The heat maps are log-scaled and scales are specific to each heatmap sub-plot. The order of the $|S(q)|$ heatmaps follows the same sweep direction denoted by the top hysteresis cycle plot (the SSF from the fully saturated regime is shown in the right hand sub-plot) Note the peaks at the corner of the Brillouin zone denoting large antiferromagnetic clusters, and coexisting with a growing peak at the center denoting magnetization.

FIG. 8: Magnetic structure factors $|S(q)|$ heatmaps within the 2D antiferromagnetic hysteresis cycles (averaged over 100 independent samples), run on `Advantage2_prototype2.6`. Each of these structure factors is from the maximum applied longitudinal field at the beginning of the first sweep, at different s pause values (different Γ/J ratios). The left most plot is from the maximum applied field region at $s = 0.6$, middle-left is at $s = 0.65$, middle-right is at $s = 0.7$, and right most is at $s = 0.8$. Note that due to the somewhat small (maximum) longitudinal field that can be applied on this QPU, these are not actually highly magnetized regions – see Figure 5 (lower right) for the average magnetization hysteresis response curves. The Ising model being simulated is a 26×26 grid of (antiferromagnetically coupled) spins, open boundary conditions. The dashed white line outlines the first Brillouin zone, and the heat maps are log-scale (with scales that are specific to each heatmap sub-plot).

Figure 11 shows that not only a staggered antiferromagnetic order parameter is different from zero, but that it also forms hysteresis cycles. Data are from experiments on `Advantage_system6.4`. Figures 12, 13, 14, show the same set of data but from the other three quantum annealing processors. The occasional hysteresis is very distinct from the the ferromagnetic-like magnetization curves seen in Figure 5, for example we see non-zero area between sweeps at $s \approx 0.75, 0.55$ in Figure 11. Interestingly, at very small Γ/J we do see long-range antiferromagnetic ordering this is expected because state

transitions are much harder when the transverse field is weak. However, the data for staggered Néel parameter is significantly noisier than average net magnetization in Figure 5. This effect could in part originate in shot noise; also, the Néel order parameter could be more sensitive to hardware biases. In future studies we will apply statistic-balancing calibration refinement [44] on the local fields and on the couplers to reduce the noise. For the three devices where full magnetic M_z saturation was reached, M_s converges entirely to zero during the hysteresis cycle for the values of s corresponding to maximal hysteretic
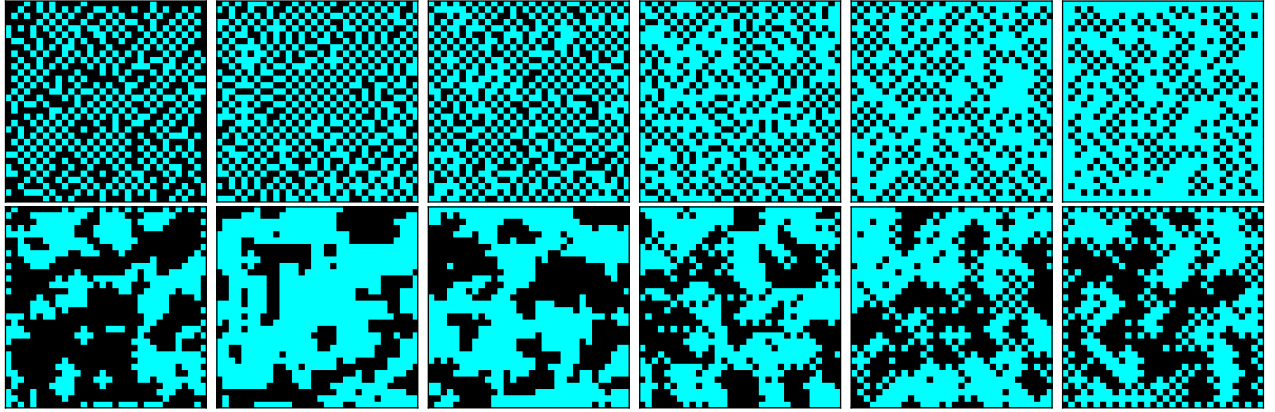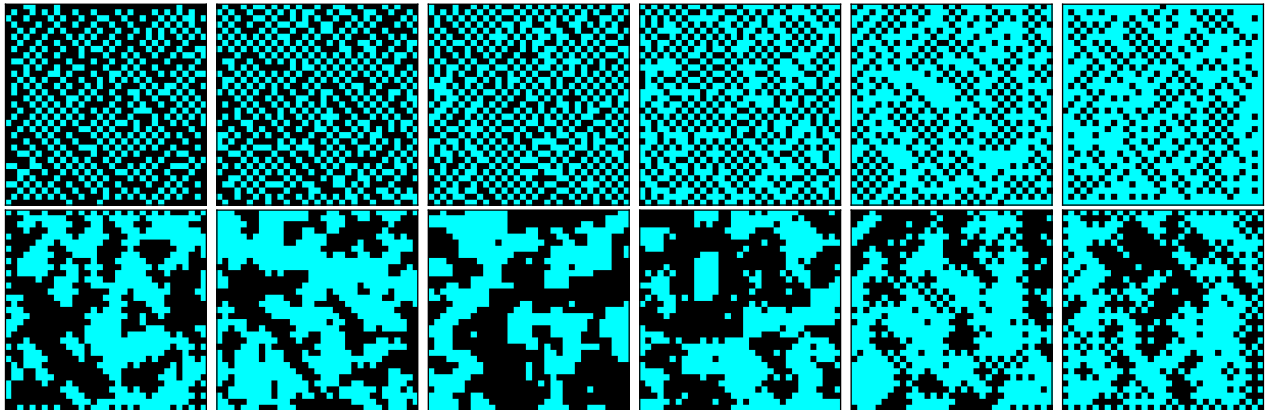
FIG. 9: Selected real-space spin configurations sampled on the `Advantage_system6.4` QPU, illustrated as pixel plots where black pixels denote spin down qubit measurements and cyan pixels denote spin up qubit measurements (top row), from the middle of the magnetization reversal at various longitudinal field strengths of the first magnetic hysteresis sweep of a 32×32 2D square grid antiferromagnet, at $s = 0.7$. Notice that the checkerboard antiferromagnetic ground-state emerges in sections of the lattices. Also notice that the boundary effects from the open boundary conditions are noticeable in many of the measured spin configurations. Bottom row: staggered domain height function τ from Eq. (13), corresponding to the same spin configurations on top, making the antiferromagnetic domains apparent.

FIG. 10: Selected real-space spin configurations sampled on the `Advantage_system7.1` QPU, illustrated as pixel plots where black pixels denote spin down qubit measurements and cyan pixels denote spin up qubit measurements (top row), from the middle of the magnetization reversal at various longitudinal field strengths of the first magnetic hysteresis sweep of a 33×33 2D square grid antiferromagnet at $s = 0.7$. Notice that the checkerboard antiferromagnetic ground-state emerges in sections of the lattices. Also notice that the boundary effects from the open boundary conditions are noticeable in many of the measured spin configurations. Bottom row: staggered domain height function τ from Eq. (13), corresponding to the same spin configurations on top, making the antiferromagnetic domains apparent.

area in M_z (see Figure 5).

C. Hysteresis Curve Areas From 1D and 2D Antiferromagnetic Hysteresis Cycles

Figure 15 plots the numerically integrated closed area of the hysteresis cycles as a function of s (equivalently, Γ/J), from the 1D and 2D antiferromagnet simulations. This shows that the region of the annealing parameter (s, equivalently Γ/J) where the hysteresis loop area is non-zero is smaller compared to the ferromagnetic models or disordered frustrated models studied in Ref. [16].

Across 1D rings and 2D grids the hysteresis loop area,

as a function of s, is non-monotonic in s: it turns on from near zero at small s, peaks in an intermediate window, and decreases again at larger s. This reflects a competition between pinning-limited reversal at low Γ/J and strong transverse-field mixing at high Γ/J, with device-to-device amplitude set primarily by the usable longitudinal field range, seen in Table I. The reduced longitudinal field produces minor loops and systematically smaller areas at the same s. In 2D, areas are further suppressed relative to 1D at matched s, consistent with reduced magnetic saturation in the 2D case.
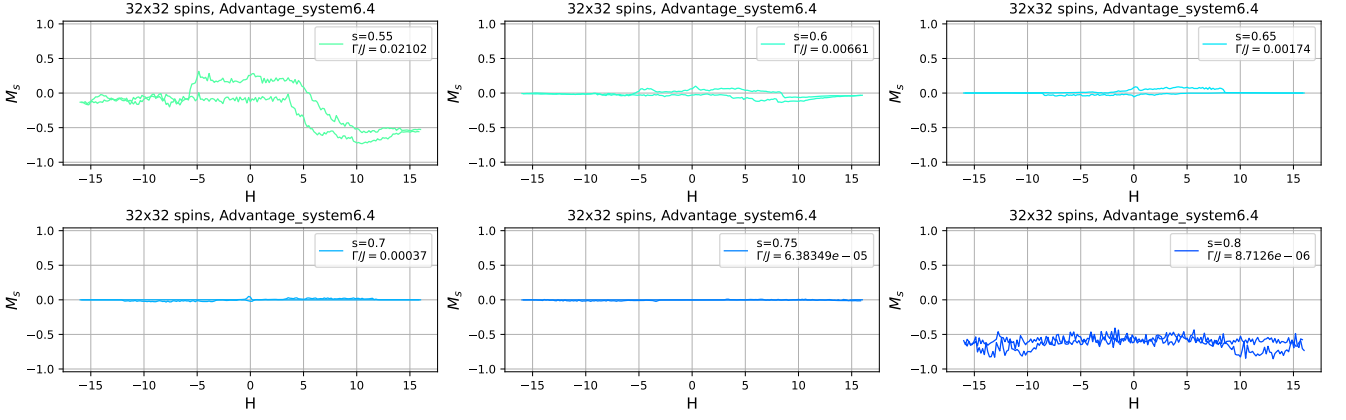
FIG. 11: 2D Hysteresis cycles in terms of the antiferromagnetic order parameter M_s. Data from `Advantage_system6.4`.
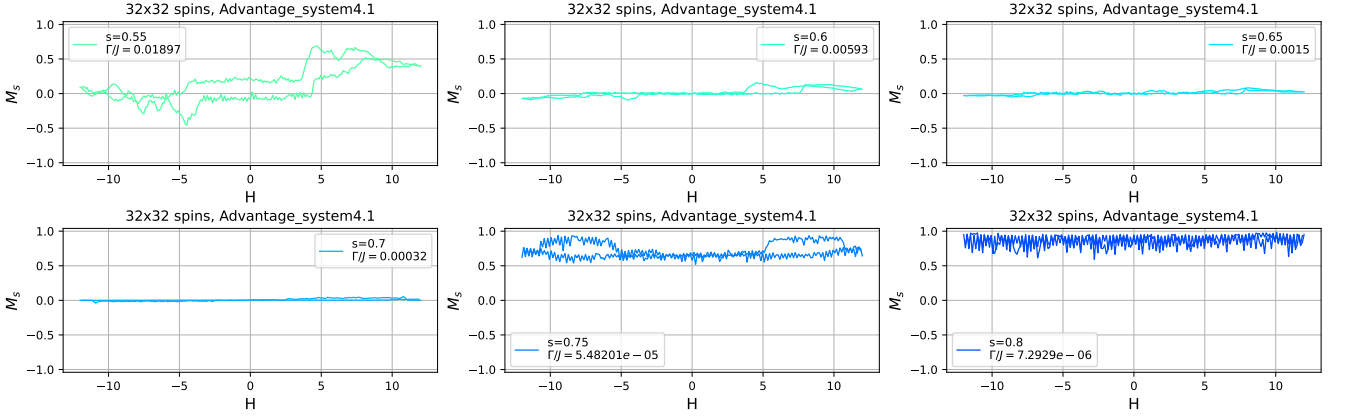

FIG. 12: 2D Hysteresis cycles in terms of the antiferromagnetic order parameter M_s. Data from `Advantage_system4.1`.
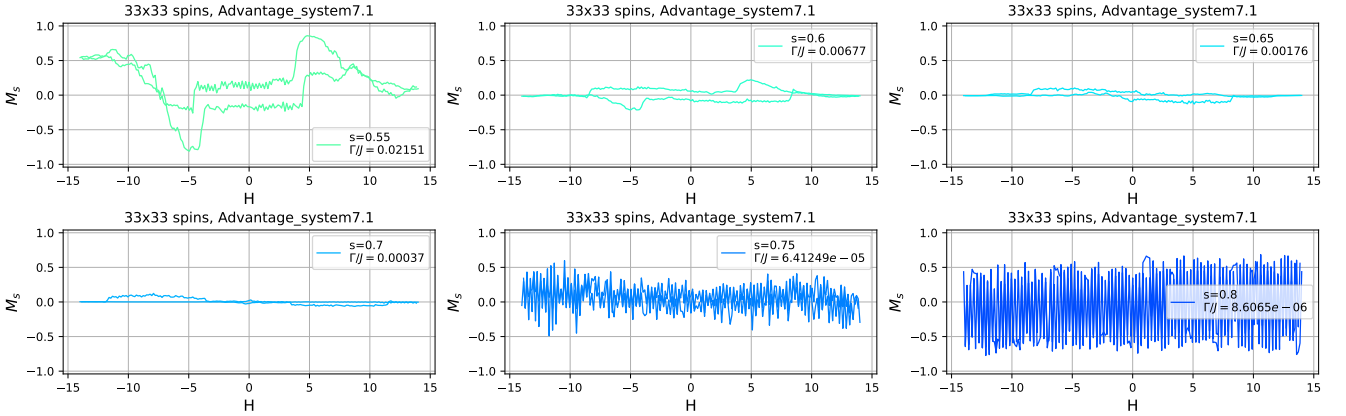

FIG. 13: 2D Hysteresis cycles in terms of the antiferromagnetic order parameter M_s. Data from `Advantage_system7.1`.

D. 3-Dimensional Antiferromagnet Experiments

Figure 16 and 17 show magnetic hysteresis simulations performed on 3D antiferromagnets – specifically these are using the entire hardware graph (every coupler being set to an antiferromagnetic coupling).

Figure 16 shows hysteresis curve data from Ising models that are *entirely antiferromagnetic.* These simula-

tions are notable because while full magnetization is not reached on any of the antiferromagnetic lattices, the non-zero transverse field does allow state transitions to take place and we recover a hysteresis curve that resembles classical ferromagnetic hysteresis. Being able to probe antiferromagnetic hysteresis using this technique is a notable computational capability given the relatively high coordination number of these graphs.
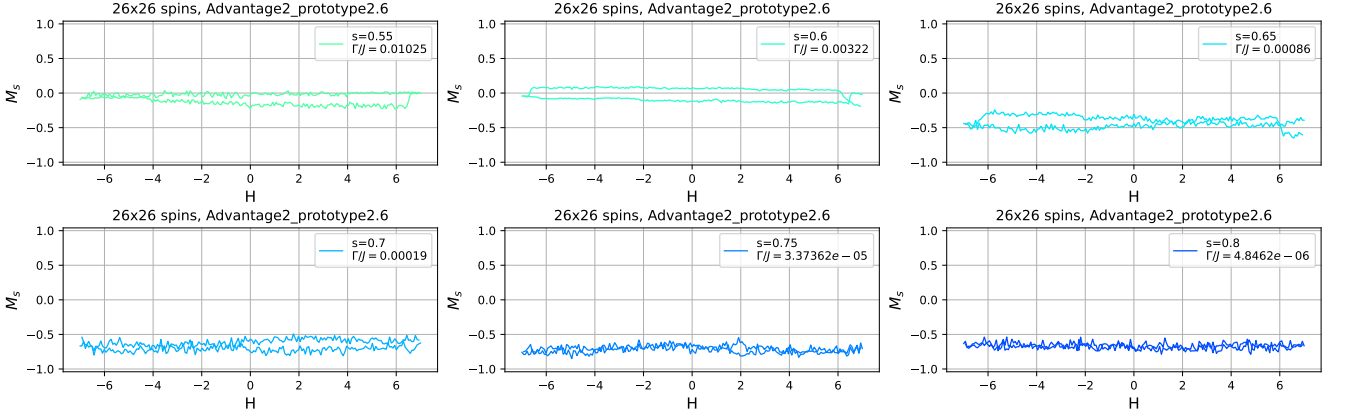
FIG. 14: 2D Hysteresis cycles in terms of the antiferromagnetic order parameter M_s. Data from `Advantage2_prototype2.6`.
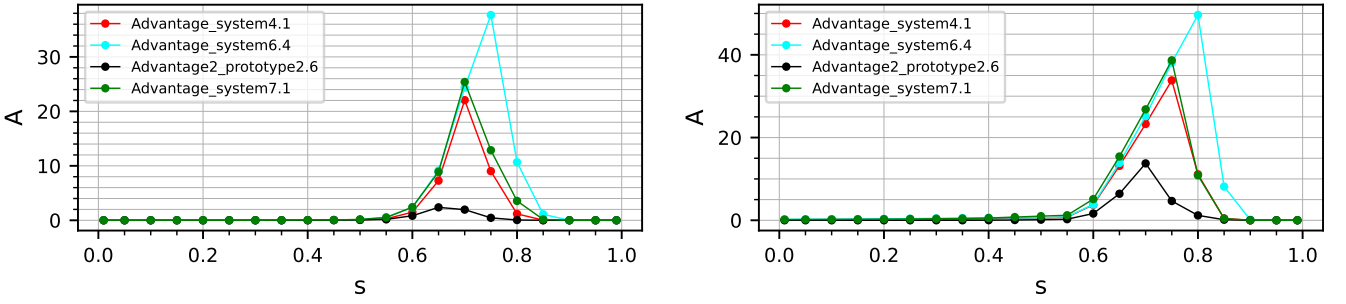

FIG. 15: Magnetic hysteresis cycle area (y-axis) versus the annealing parameter s at which the hysteresis is performed, for the 2D square antiferromagnetic square lattice with open boundaries, (left) and 1D antiferromagnetic rings, with periodic boundary conditions (right).

The general trend that we observe here is that as the coordination number of the antiferromagnetic Ising models increases, it becomes harder to fully magnetize the systems in the analog QPU simulation. This is to be expected, because higher coordination number means more energy is required, in this case a stronger longitudinal field, in order to flip the spins against the strong J lattice coupling.

1. Suppressed hysteresis in 3D Hardware Lattice

Our 3D results exhibit only small, often near–minor loops. In highly connected antiferromagnetic graphs large interfacial cost set by the coordination number and J, as a result there is limited mobility when the transverse field Γ is either too small (frozen) or too large (paramagnetic).

On an average c-coordinated AF lattice/graph, any domain surface cuts a number of bonds proportional to c per unit area. Each cut bond contributes an energy scale $\sim J$, so the effective surface tension obeys

$$\lambda \propto cJ,$$

up to geometric factors set by the lattice or embedding.

In three dimensions, the excess energy of a droplet, assumed nearly spherical, of reversed Néel order with radius R is well approximated by a surface term that scales as

$$E_{\text{surf}}(R) \simeq 4\pi\lambda R^2.$$

Higher coordination therefore stiffens domain surfaces and penalizes both surface translation and the creation of new droplets.

A longitudinal field h favors spins aligned with its sign. Flipping a spin gains Zeeman energy $2|h|$ (in our $\sigma^z = \pm 1$ normalization), so a droplet containing a volume $\frac{4}{3}\pi R^3$ gains

$$E_{\text{field}}(R) \simeq -\tfrac{4}{3}\pi R^3 (2|h|m_0), \tag{14}$$

where m_0 is the net spin per site in the ordered domain (for perfectly staggered order $m_0 = 1$ in our units). The competition of the two terms yields a critical radius

$$R_c = \frac{2\lambda}{2|h|m_0} = \frac{\lambda}{|h|m_0}, \tag{15}$$

and an activation barrier

$$E_c = E_{\text{surf}}(R_c) + E_{\text{field}}(R_c) = \frac{2\pi}{3}\frac{\lambda^3}{|h|^2 m_0^2}. \tag{16}$$
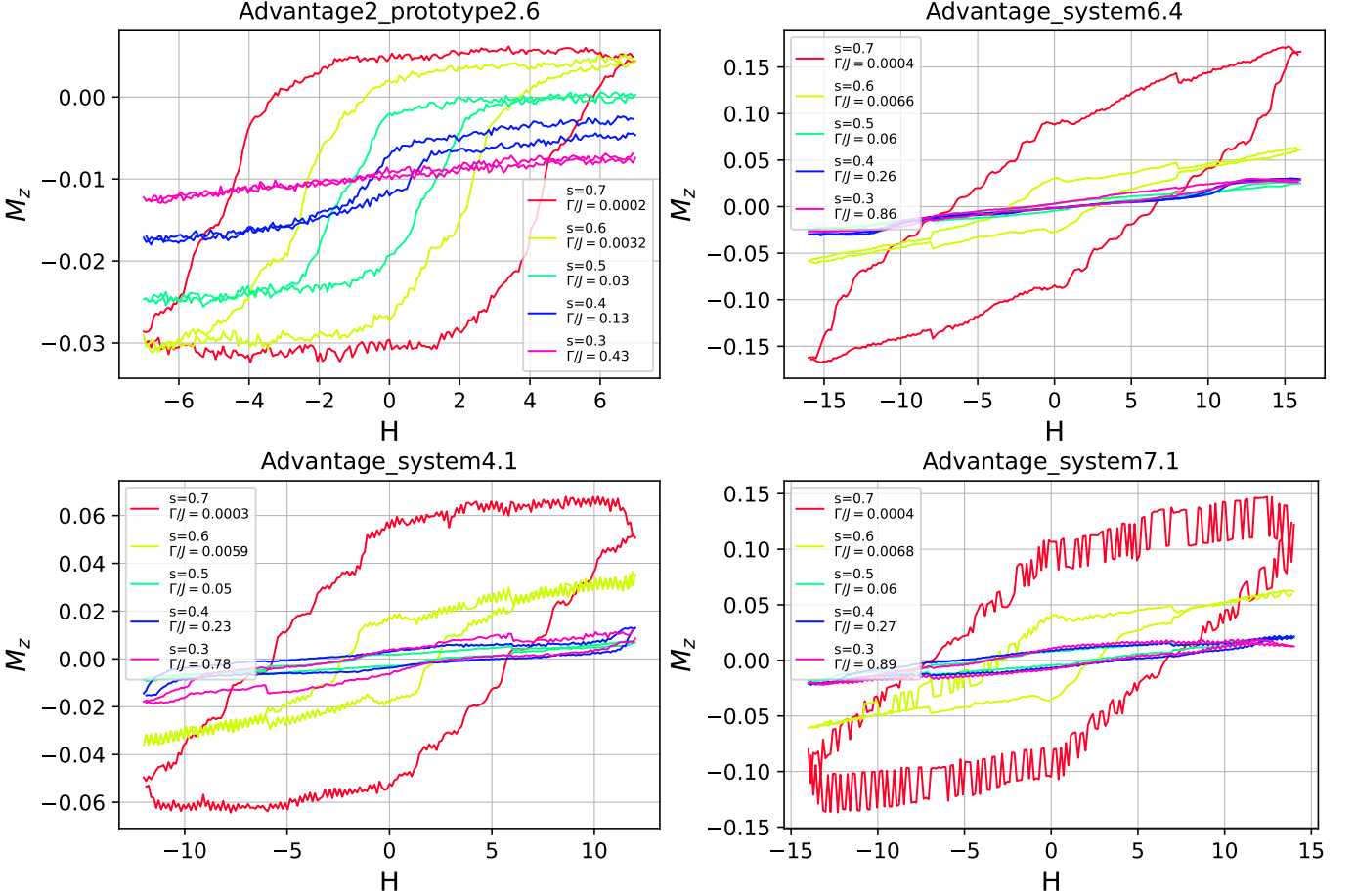
FIG. 16: Magnetic hysteresis of 3D hardware-defined antiferromagnets, with no calibration refinement. Average magnetization (y-axis) as a function of the applied longitudinal field (x-axis). Because the absolute range of magnetization (y-axis) is much smaller than the other Ising models, here we increase the shot count (e.g., the total number of samples obtained by a complete anneal-readout cycle) to 8000 for each datapoint. This increase in the number of samples reduces local jitter of the magnetization curves. No flux bias offset calibration was used for these simulations (e.g., before calibration). The overlaid black arrows on the average magnetization lines sampled from the QPUs simultaneously denote the time-progression of the analog simulations, as well as the direction of the longitudinal field sweeps.

Thus in 3D the surface-area cost increases both R_c and E_c sharply, in addition the high hardware-coordination c raises λ and therefore pushes R_c and E_c up, suppressing bulk nucleation across the sweep range we employ.

On finite samples, droplets can nucleate as caps on faces (roughly halving both surface and volume terms) or at edges/corners (reducing cost further). This boundary-assisted nucleation produces small droplets and corresponding small hysteresis. Most field steps only rattle pinned facets without producing large, hysteretic changes in M_z.

The interfacial picture also clarifies how the control knobs set the loop morphology. First, the sweep amplitude (envelope) determines whether droplets can ever become supercritical: if the field never reaches values for which the critical radius R_c is microscopic, nucleation remains subcritical and the response collapses to minor, low-area cycles. Second, the sweep rate and dwell time control the opportunity for rare, multi-spin pro-

cesses that assist nucleation and for marginal droplets to grow: faster ramps and shorter dwells reduce this opportunity and thus diminish loop area. Third, the transverse field fixes the matrix element for local surface moves and pair creation; for $\Gamma/J \ll 1$ surfaces are effectively frozen, while for very large Γ/J strong quantum mixing erases memory of the sweep path so that hysteresis collapses. A pronounced, reproducible loop therefore occurs only in an intermediate window of Γ/J that is large enough to enable surface translation across pinning sites but not so large as to randomize domains during the protocol.

IV. DISCUSSION AND CONCLUSION

We have demonstrated for the first time large-scale simulations of antiferromagnetic hysteresis using quantum computers. This includes observation of unexpected non-monotonic magnetization curves as has been seen
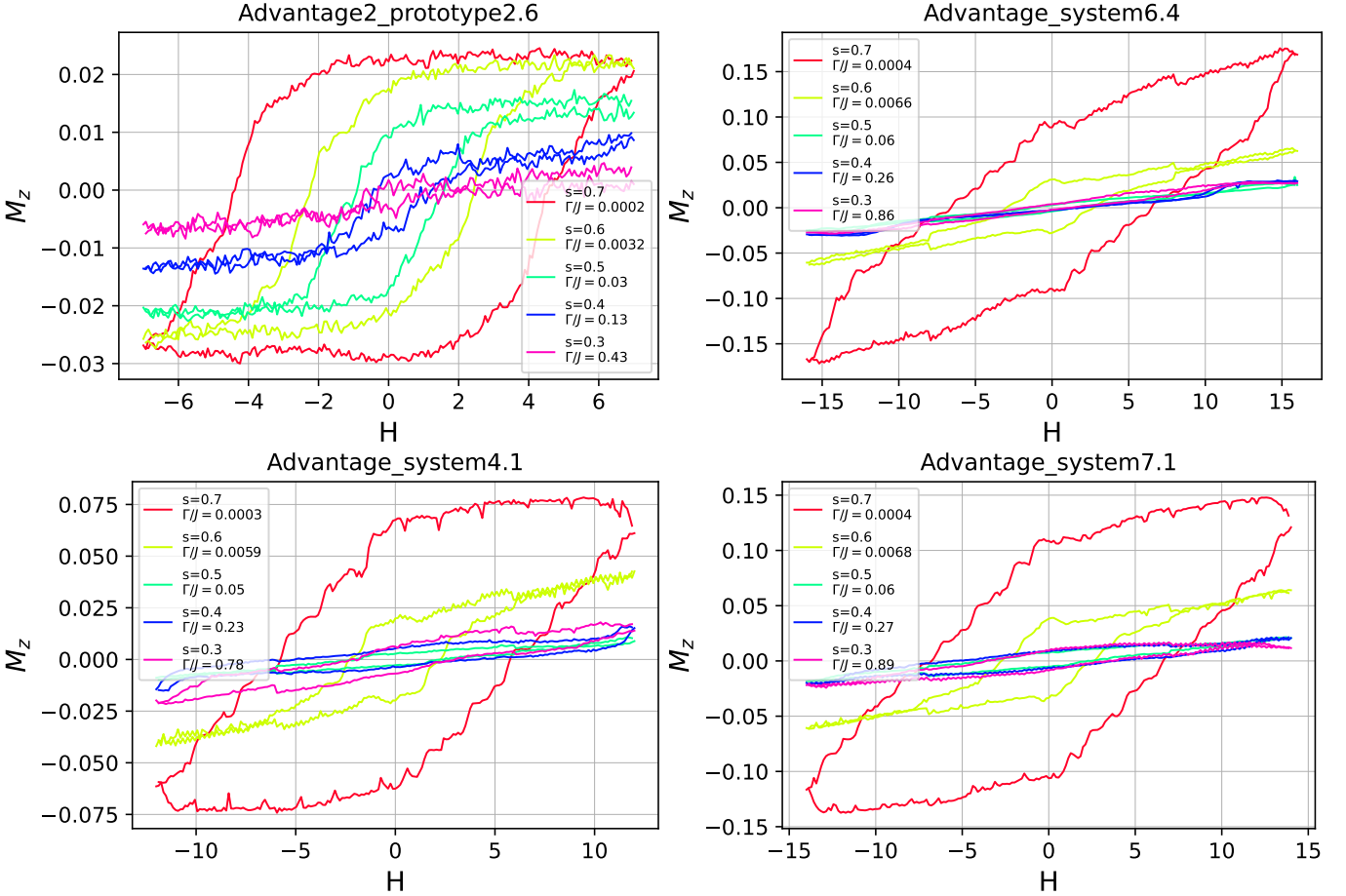
FIG. 17: **Magnetic hysteresis on hardware-defined antiferromagnets, with extensive whole-lattice FBO calibration refinement**. Average magnetization (y-axis) as a function of the applied longitudinal field (x-axis). Each datapoint on the hysteresis curves are averaged single site magnetization from 8000 samples. In comparison to Figure 16 where no statistic balancing calibration was used, here we see in general smoother magnetization curves, in particular on the `Advantage_system7.1` processor.

before in these types of analog QPU simulations on 1D ferromagnets [17], along with extraction of spin structure factor showing clear transitions of magnetic ordering during the hysteresis cycles. The structure factor plots show clear antiferromagnetic ordering transition from ferromagnetic like ordering when the systems are fully polarized, as well as boundary effects. We have also demonstrated that the use of statistic-balancing calibration on the analog quantum hardware can improve the quality of the hysteresis simulations, as demonstrated on full-hardware-graph antiferromagnets. One of the primary results that we demonstrate is that for low coordination antiferromagnets (1D and 2D Ising models in particular), under an appropriately tuned ratio of transverse field (Γ) to lattice coupling (J), we can achieve full polarization of the antiferromagnets. Furthermore, the subsequent reversal resembles many of the key features of standard classical hysteresis in disordered, and even ferromagnetic, spin systems.

Our measurements establish robust dynamical hysteresis in programmable antiferromagnets across geome-

tries. In 1D odd rings, a built-in domain wall yields reproducible, step-like reversal under a transverse field. In 2D finite samples, boundary-assisted switching and droplet growth are consistent with the observed evolution of the spin-structure factor. The highly coordinated hardware graphs suppress the ferromagnetic ordering, producing weak, near-minor loops. Overall, loop morphology is set by a small set of tunable parameters—geometry and coordination, the sweep protocol, and the ratio Γ/J—highlighting quantum annealers as controllable platforms for exploring nonequilibrium antiferromagnetic dynamics.

Interestingly, some of the hysteresis simulations we present in this study share some qualities with measured magnetic hysteresis cycles in certain molecular magnets [58]. Similarities between these analog open-quantum system hysteresis simulations to molecular magnetic hysteresis deserves further investigation.

Future work can explore the dynamical origin of this hysteresis, its potential relationship with the qubit quantum dynamics, and also establish a closer connection with

real magnetic materials and compare results from quantum annealers to those from laboratory experiments. Future study should also investigate additional calibrated antiferromagnetic hysteresis cycle simulations (in particular of the couplers and of the flux bias offsets), in particular on the 2-dimensional systems where the antiferromagnetic order parameter data shows much more statistical fluctuations.

This computational capability of near term analog quantum computers highlights that the full programmability of these devices inherently gives us the capability to examine phenomena which are hard to systematically study in magnetic laboratories – in this case, antiferromagnetic hysteresis.
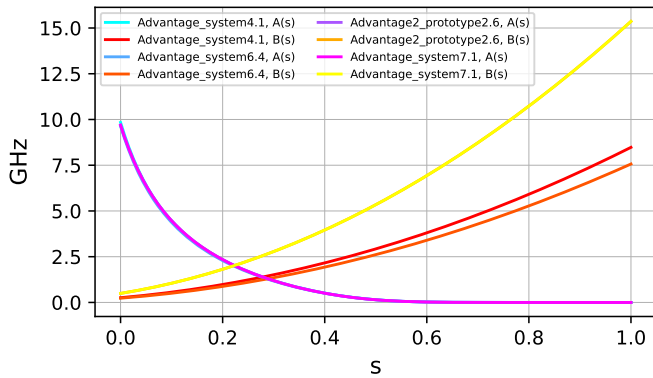
FIG. 18: overlaid $A(s)$ and $B(s)$ hardware specific functions for the 4 D-Wave QPUs used in this study.

Appendix A: D-Wave Hardware $A(s)$ and $B(s)$ Functions

Figure 18 plots the $A(s)$ and $B(s)$ schedules, that define the D-Wave hardware Hamiltonian in eq. (1), which allows us to then define physical ratios such as Γ/J. This is important specifically because all of the programmable units on the D-Wave QPUs are specified in terms of hardware-normalized parameters, and therefore it is necessary to extract the correct energy scales of the D-Wave anneal-schedules to show where certain features of the magnetic hysteresis protocols appear in physical units, for example at what applied field does magnetization reversal begin. Note that these frequencies are not in angular frequency units.

Appendix B: Flux Bias Offset Balancing Calibration

Due to the analog nature of the D-Wave quantum annealing hardware, it can be beneficial to calibrate the statistics of physical quantities that can be measured from the annealing simulations. In particular, analog errors and thermal effects can result in biased quantities. In this study we make use of a particular type of calibration procedure which balances the statistics obtained from the full-hardware-lattice-antiferromagnets. The update procedure used follows ref. [44], and in particular is effectively a type of parallel-update steepest gradient descent machine learning process, and is very much an *autonomous* analog control correction procedure. This is reminiscent of gradient descent approaches in the training of neural networks [59, 60]. The hardware control mechanism that is used here is the flux bias offset (FBO) control of each individual qubit [61] which can force the qubit to be biased towards spin up or down, and in this case we very slightly update the FBO proportionally to the size of the bias of the single-qubit magnetization (relative to the mean of the distribution across all qubits). The update procedure used follows ref. [44], and in particular is effectively a type of parallel-update steepest gradient descent process. This is reminiscent of gradient descent approaches in the training of neural networks [59, 60]. The statistics balancing method in particular makes use of a correction towards the mean sampled observable (M_z) across all spins; in this case, we expect the net average magnetization to be zero, and the non-calibrated distributions also have a mean of approximately zero, which makes this correction method work quite well in this case because its primary action is to reduce the variance of the measured single-spin magnetization on the lattice. The magnetization FBO update is relatively easy to perform because all of the qubits are in the same observable "orbit" [44], meaning we expect on average the magnetization of each qubit to be the same as all of the other qubits. Note however that this balancing did not adjust the J antiferromagnetic couplers; refining the programmed coupler energy values is possible to adjust as well, however boundaries in the lattice mean that different observable orbits must be constructed – which for the specific case of the highly complex hardware graphs would make the calibration significantly more computationally intensive in terms of total
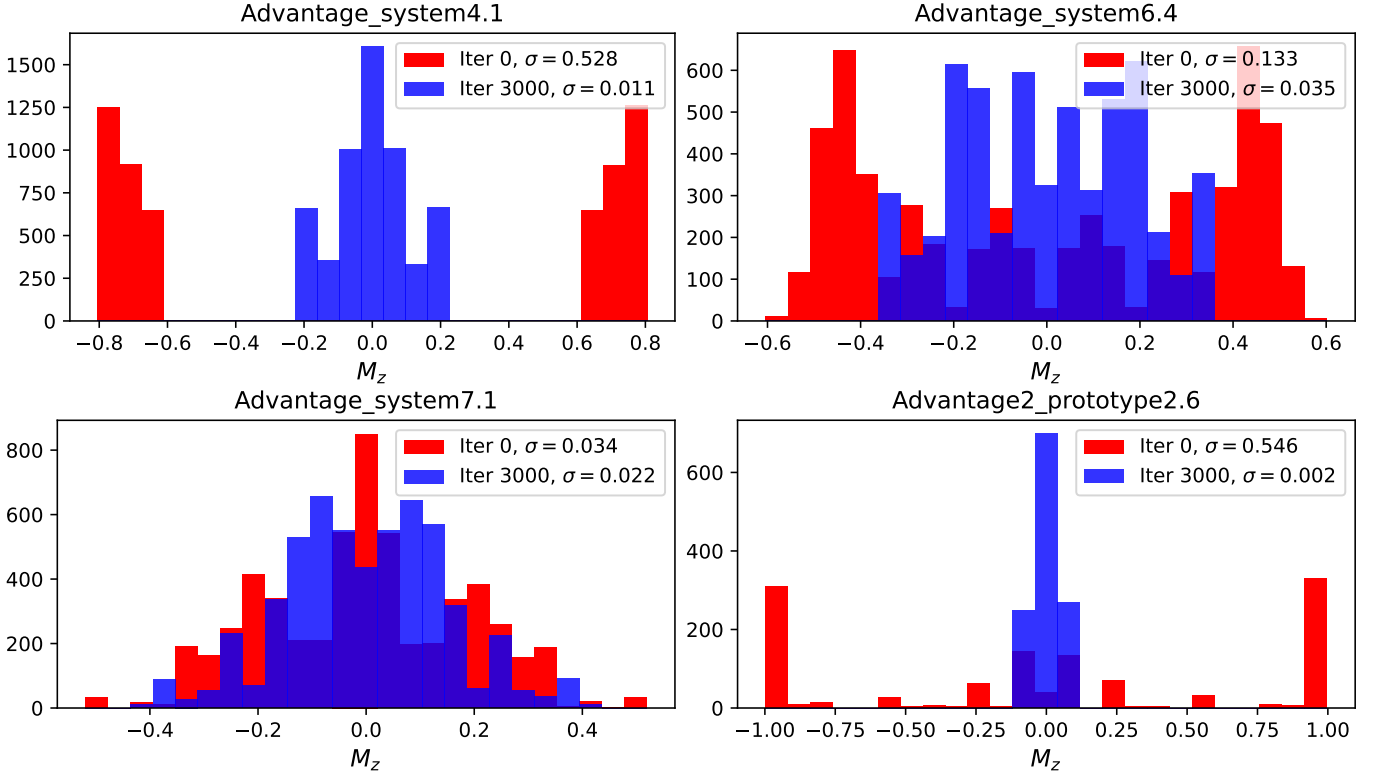
FIG. 19: Single site magnetization distributions, for each qubit in the hardware lattice, before flux bias offset calibration and after calibration for a full antiferromagnetic lattice defined on the entire hardware graph. 3000 gradient descent steps were used in total, and the flux bias offset stepsize is $2e^{-6}$ (with initial flux bias offset being uniformly zero). The standard deviation of the distribution of average single-site magnetization before (iteration 0) and after (iteration 3000) the FBO calibration is notated in the legend – in all cases we see a decrease in the variance of the single-site magnetization distribution, which is the goal of the statistic balancing process. Each iteration of this calibration process, on each QPU, uses exactly 3000 samples. The flux bias offset quantity calibration is shown in Figure 20.

iterations and also parameter tuning. Therefore, we focused on FBO calibration, which yielded improved magnetization curve stability.

Figure 19 shows the distribution of average magnetization per spin both before and after FBO statistic-balancing calibration. Figure 20 plots the values of the flux bias offsets, for every qubit in the hardware graph, as a function of update iteration, which in this case we terminate at a fixed iteration count of 3000 in order to make the simulations tractable in terms of compute time, and real-time backend usage. The flux bias offset constant step-size used was $2e^{-6}$ (the actual update is proportional to the magnitude of the bias, and this is the constant by which the bias is multiplied by). This specific stepsize we found worked reasonably well from small scale empirical testing; larger stepsizes could in principle correct biases more quickly, but over-correction and thereby numerical instability in the convergence was frequently observed for step sizes larger than $\approx 2e^{-6}$. The calibrated FBOs used in the subsequently hysteresis computations are simply the FBOs in the final learning iteration. Time drift in an important consideration in these D-Wave QPU computations (over long periods of time, D-Wave simulations do change measurably [36]),

and therefore the complete set of hysteresis cycle data using the calibrated FBO values (shown in Figure 17) were run within 48 hours of this calibration, with the aim of minimizing the effect of noise drift. At each update step, a total of 3000 anneal-readout cycles were performed (all in one device job call), and the subsequent update is performed using the (average) magnetization values for every site on the hardware lattice using all 3000 samples. Importantly, the anneal-schedule used in this calibration procedure *was not* the hysteresis protocol – there was no anneal-pause, and no h-gain field. Instead, this calibration was performed only on the standard linear-ramp anneal schedule, using the final simulation time in the hysteresis protocol (in this case, always $11.2\mu s$). This means the same FBO calibration (after the 3000 learning iterations), for each QPU, was used for each Γ/J and each "slice" of the longitudinal field ramps. More advanced calibration, and more QPU time intensive, could specifically calibrate each Γ/J, and each longitudinal field sweep step. Interestingly, Figure 19 shows that some of the D-Wave processors are much easier to calibrate, presumably meaning they are less noisy, such as `Advantage_system4.1`, whereas `Advantage_system7.1` appears to be the most
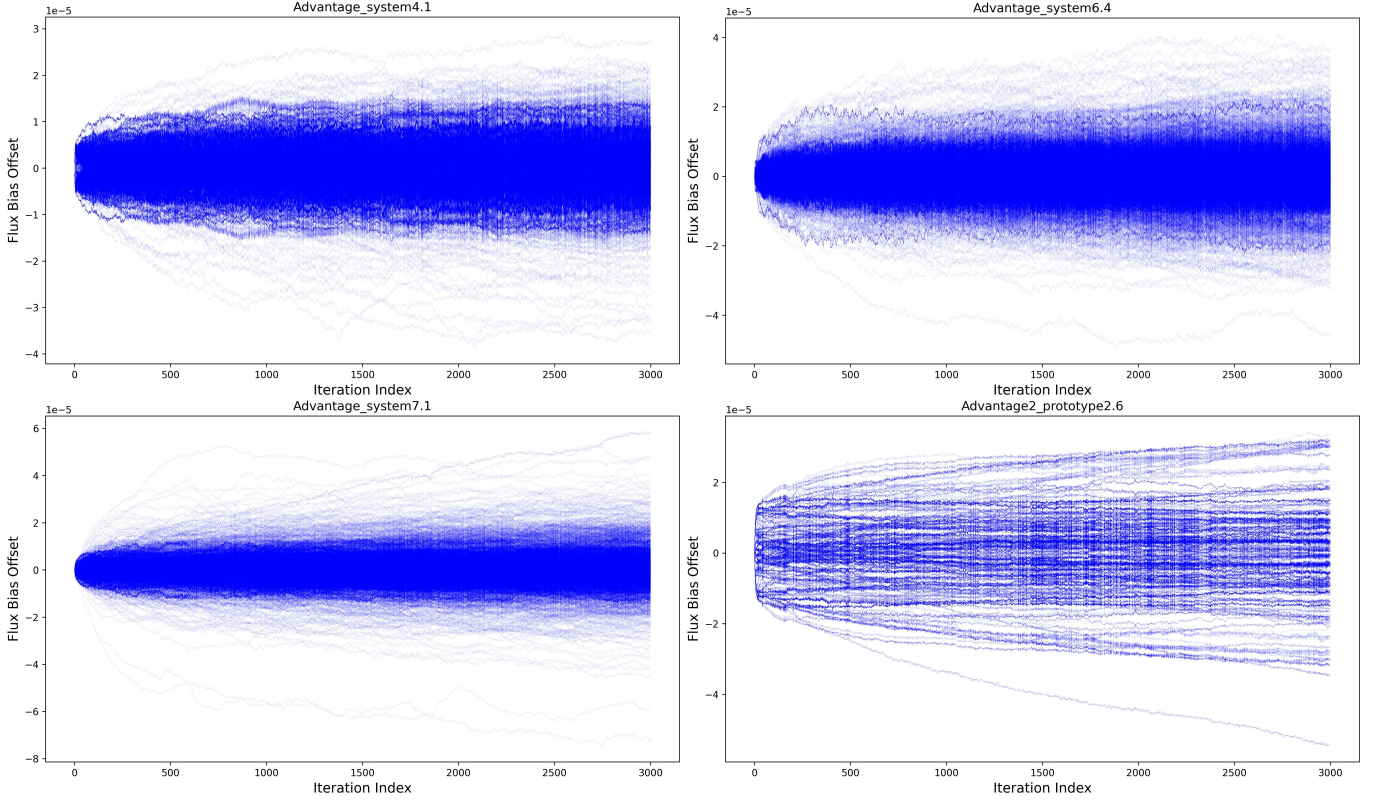
FIG. 20: Evolution of FBO values, for each single qubit in the hardware-lattice, as the calibration process evolves up to 3000 iterations. The Ising model being sampled during this calibration is a full antiferromagnet defined lattice, using every coupler of each of the D-Wave hardware graphs. The initial flux bias offset starts at all zeroes for all qubits, and each iteration has a maximum FBO stepsize of $2e^{-6}$.

noisy and also exhibited the least de-biasing when this calibration protocol was applied as evidenced by having the widest magnetization distribution variance post-calibration. This is also indicated by the flux bias offset quantities as a function of iteration in Figure 20 – we see that specifically in the case of `Advantage_system7.1` and `Advantage2_prototype2.6`, some of the qubits did not converge in their FBO values, whereas `Advantage_system4.1` and `Advantage_system6.4` appear to have converged more quickly.

Appendix C: Additional Representative Magnetic Spin Structure Factors

This section provides several additional sequences of averaged magnetic structure factors at various points along various 2D antiferromagnetic hysteresis simulations; Figure 21, Figure 22, Figure 23, Figure 24, Figure 25, Figure 26, each from different hysteresis cycles at various s values and run on the two different Pegasus processors. In these structure factors, effects from the open boundary conditions and finite lattice are prominent, especially at full saturation. In the less saturated regions of the hysteresis cycles, the antiferromagnetic ordering becomes apparent with peaks at (π, π) in the square lattice.
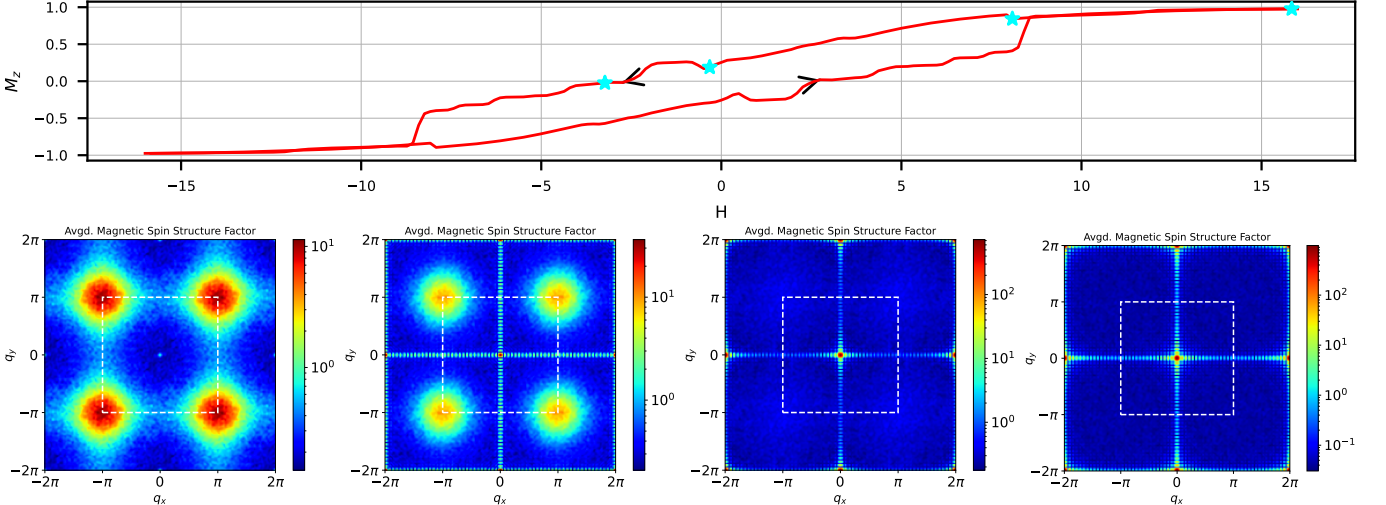
FIG. 21: Magnetic structure factors $|S(q)|$ heatmaps (bottom row) within the 2D antiferromagnetic hysteresis cycles (averaged over 100 independent samples), run on `Advantage_system6.4` at $s = 0.65$. The Ising model being simulated is a 32×32 grid of (antiferromagnetically coupled) spins, open boundary conditions. Left-most sub-plots show hysteresis simulation in the approximately de-magnetized region, where the antiferromagnetic ordering becomes clearer. The dashed white line outlines the first Brillouin zone, and the heat maps are log-scale (with scales that are specific to each heatmap sub-plot). The top row shows the single hysteresis cycle in terms of M_z average magnetization, from which we extracted $|S(q)|$ heatmaps for 4 points along the first longitudinal field sweep, denoted by cyan asterisks. The order of the $|S(q)|$ heatmaps follows the same sweep direction denoted by the top hysteresis cycle plot (the SSF from the fully saturated regime is shown in the right hand sub-plot).
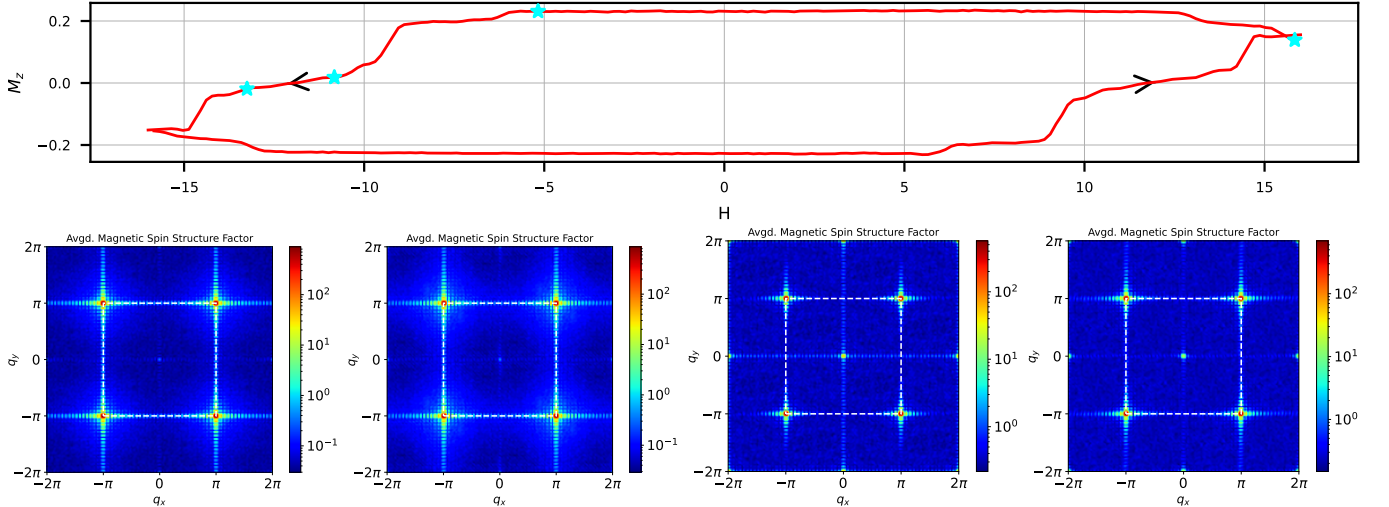

FIG. 22: Magnetic structure factors $|S(q)|$ heatmaps (bottom row) within the 2D antiferromagnetic hysteresis cycles (averaged over 100 independent samples), run on `Advantage_system6.4` at $s = 0.8$. The Ising model being simulated is a 32×32 grid of (antiferromagnetically coupled) spins, open boundary conditions. Left-most sub-plots show hysteresis simulation in the approximately de-magnetized region, where the antiferromagnetic ordering becomes clearer. The dashed white line outlines the first Brillouin zone, and the heat maps are log-scale (with scales that are specific to each heatmap sub-plot). The top row shows the single hysteresis cycle in terms of M_z average magnetization, from which we extracted $|S(q)|$ heatmaps for 4 points along the first longitudinal field sweep, denoted by cyan asterisks. The order of the $|S(q)|$ heatmaps follows the same sweep direction denoted by the top hysteresis cycle plot (the SSF from the fully saturated regime is shown in the right hand sub-plot).
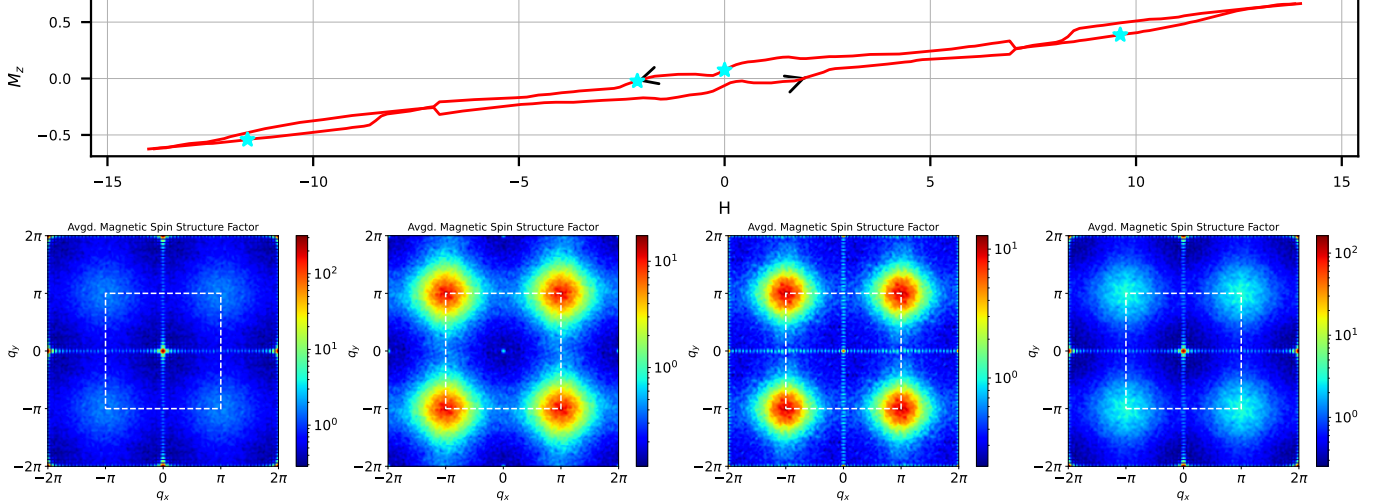
FIG. 23: Magnetic structure factors $|S(q)|$ heatmaps (bottom row) within the 2D antiferromagnetic hysteresis cycles (averaged over 100 independent samples), run on `Advantage_system7.1` at $s = 0.6$. The Ising model being simulated is a 33×33 grid of (antiferromagnetically coupled) spins, open boundary conditions. Left-most sub-plots show hysteresis simulation in the approximately de-magnetized region, where the antiferromagnetic ordering becomes clearer. The dashed white line outlines the first Brillouin zone, and the heat maps are log-scale (with scales that are specific to each heatmap sub-plot). The top row shows the single hysteresis cycle in terms of M_z average magnetization, from which we extracted $|S(q)|$ heatmaps for 4 points along the first longitudinal field sweep, denoted by cyan asterisks. The order of the $|S(q)|$ heatmaps follows the same sweep direction denoted by the top hysteresis cycle plot (the SSF from the fully saturated regime is shown in the right hand sub-plot).

FIG. 24: Magnetic structure factors $|S(q)|$ heatmaps (bottom row) within the 2D antiferromagnetic hysteresis cycles (averaged over 100 independent samples), run on `Advantage_system4.1` at $s = 0.7$. The Ising model being simulated is a 32×32 grid of (antiferromagnetically coupled) spins, open boundary conditions. Left-most sub-plots show hysteresis simulation in the approximately de-magnetized region, where the antiferromagnetic ordering becomes clearer. The dashed white line outlines the first Brillouin zone, and the heat maps are log-scale (with scales that are specific to each heatmap sub-plot). The top row shows the single hysteresis cycle in terms of M_z average magnetization, from which we extracted $|S(q)|$ heatmaps for 4 points along the first longitudinal field sweep, denoted by cyan asterisks. The order of the $|S(q)|$ heatmaps follows the same sweep direction denoted by the top hysteresis cycle plot (the SSF from the fully saturated regime is shown in the right hand sub-plot).
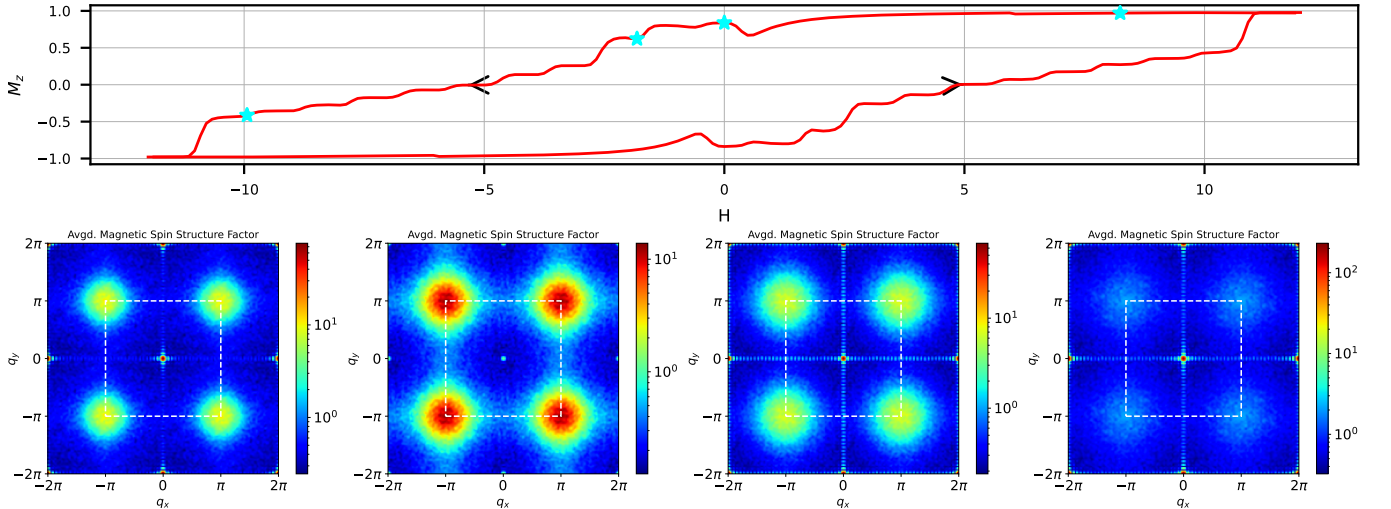
FIG. 25: Magnetic structure factors $|S(q)|$ heatmaps (bottom row) within the 2D antiferromagnetic hysteresis cycles (averaged over 100 independent samples), run on `Advantage_system4.1` at $s = 0.65$. The Ising model being simulated is a 32×32 grid of (antiferromagnetically coupled) spins, open boundary conditions. Left-most sub-plots show hysteresis simulation in the approximately de-magnetized region, where the antiferromagnetic ordering becomes clearer. The dashed white line outlines the first Brillouin zone, and the heat maps are log-scale (with scales that are specific to each heatmap sub-plot). The top row shows the single hysteresis cycle in terms of M_z average magnetization, from which we extracted $|S(q)|$ heatmaps for 4 points along the first longitudinal field sweep, denoted by cyan asterisks. The order of the $|S(q)|$ heatmaps follows the same sweep direction denoted by the top hysteresis cycle plot (the SSF from the fully saturated regime is shown in the right hand sub-plot).
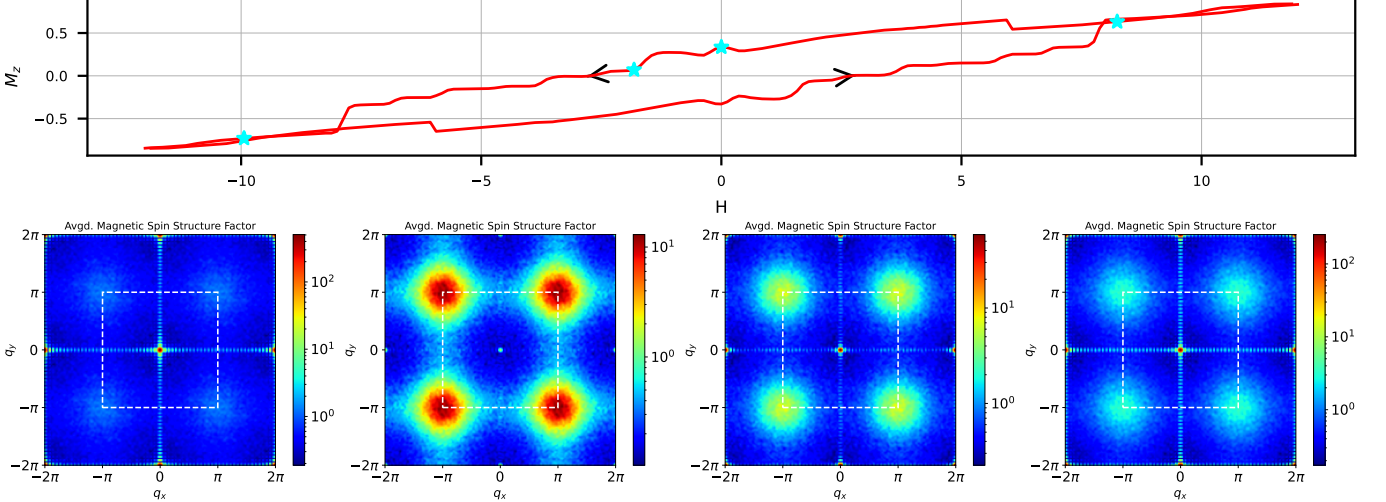

FIG. 26: Magnetic structure factors $|S(q)|$ heatmaps (bottom row) within the 2D antiferromagnetic hysteresis cycles (averaged over 100 independent samples), run on `Advantage_system7.1` at $s = 0.65$. The Ising model being simulated is a 33×33 grid of (antiferromagnetically coupled) spins, open boundary conditions. Left-most sub-plots show hysteresis simulation in the approximately de-magnetized region, where the antiferromagnetic ordering becomes clearer. The dashed white line outlines the first Brillouin zone, and the heat maps are log-scale (with scales that are specific to each heatmap sub-plot). The top row shows the single hysteresis cycle in terms of M_z average magnetization, from which we extracted $|S(q)|$ heatmaps for 4 points along the first longitudinal field sweep, denoted by cyan asterisks. The order of the $|S(q)|$ heatmaps follows the same sweep direction denoted by the top hysteresis cycle plot (the SSF from the fully saturated regime is shown in the right hand sub-plot).
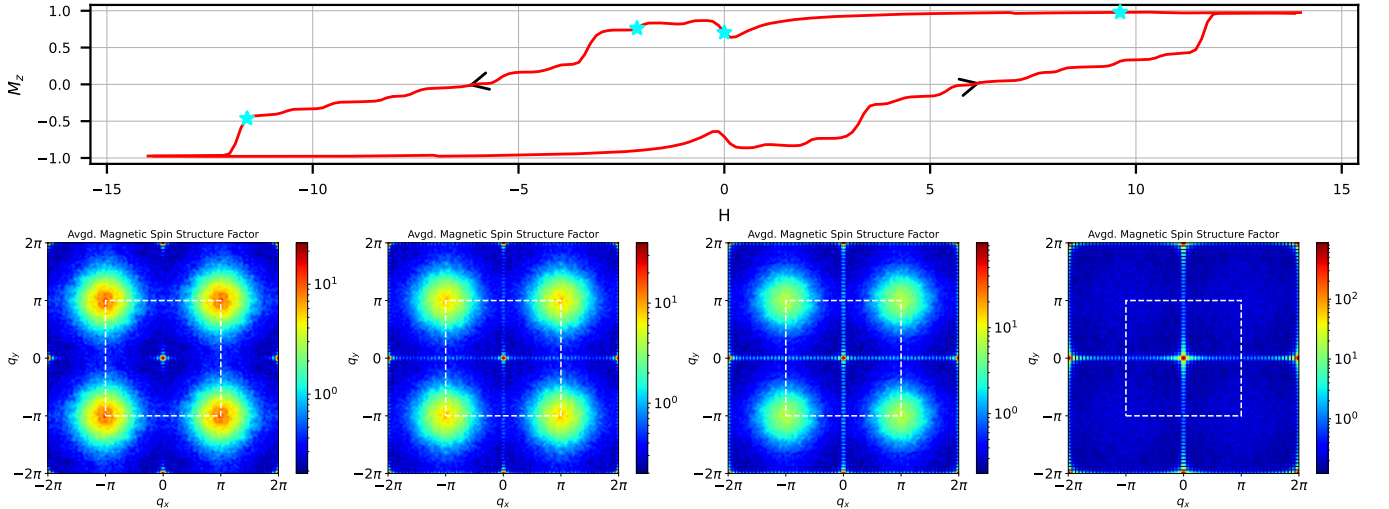
[1] S. Morita and H. Nishimori, *Mathematical foundation of quantum annealing*, Journal of Mathematical Physics **49**, 10.1063/1.2995837 (2008).

[2] E. Farhi, J. Goldstone, S. Gutmann, and M. Sipser, Quantum Computation by Adiabatic Evolution (2000), arXiv:quant-ph/0001106 [quant-ph].

[3] G. E. Santoro, R. Martoňák, E. Tosatti, and R. Car, *Theory of Quantum Annealing of an Ising Spin Glass*, Science **295**, 2427–2430 (2002).

[4] T. Kadowaki and H. Nishimori, *Quantum annealing in the transverse ising model*, Physical Review E **58**, 5355–5363 (1998), arXiv:cond-mat/9804280.

[5] A. D. King, C. D. Batista, J. Raymond, T. Lanting, I. Ozfidan, G. Poulin-Lamarre, H. Zhang, and M. H. Amin, *Quantum Annealing Simulation of Out-of-Equilibrium Magnetization in a Spin-Chain Compound*, PRX Quantum **2**, 030317 (2021).

[6] R. Harris, Y. Sato, A. J. Berkley, M. Reis, F. Altomare, M. Amin, K. Boothby, P. Bunyk, C. Deng, C. Enderud, *et al.*, *Phase transitions in a programmable quantum spin glass simulator*, Science **361**, 162–165 (2018).

[7] S. N. Hearth, S. C. Morampudi, and C. R. Laumann, *Quantum orders in the frustrated ising model on the bathroom tile lattice*, Phys. Rev. B **105**, 195101 (2022).

[8] A. D. King, J. Carrasquilla, J. Raymond, I. Ozfidan, E. Andriyash, A. Berkley, M. Reis, T. Lanting, R. Harris, F. Altomare, K. Boothby, P. I. Bunyk, C. Enderud, A. Fréchette, E. Hoskinson, N. Ladizinsky, T. Oh, G. Poulin-Lamarre, C. Rich, Y. Sato, A. Y. Smirnov, L. J. Swenson, M. H. Volkmann, J. Whittaker, J. Yao, E. Ladizinsky, M. W. Johnson, J. Hilton, and M. H. Amin, *Observation of topological phenomena in a programmable lattice of 1,800 qubits*, Nature **560**, 456–460 (2018).

[9] A. D. King, C. Nisoli, E. D. Dahl, G. Poulin-Lamarre, and A. Lopez-Bezanilla, *Qubit spin ice*, Science **373**, 576–580 (2021).

[10] A. D. King, A. Nocera, M. M. Rams, J. Dziarmaga, R. Wiersema, W. Bernoudy, J. Raymond, N. Kaushal, N. Heinsdorf, R. Harris, K. Boothby, F. Altomare, A. J. Berkley, M. Boschnak, K. Chern, H. Christiani, S. Cibere, J. Connor, M. H. Dehn, R. Deshpande, S. Ejtemaee, P. Farré, K. Hamer, E. Hoskinson, S. Huang, M. W. Johnson, S. Kortas, E. Ladizinsky, T. Lai, T. Lanting, R. Li, A. J. R. MacDonald, G. Marsden, C. C. McGeoch, R. Molavi, R. Neufeld, M. Norouzpour, T. Oh, J. Pasvolsky, P. Poitras, G. Poulin-Lamarre, T. Prescott, M. Reis, C. Rich, M. Samani, B. Sheldan, A. Smirnov, E. Sterpka, B. T. Clavera, N. Tsai, M. Volkmann, A. Whiticar, J. D. Whittaker, W. Wilkinson, J. Yao, T. J. Yi, A. W. Sandvik, G. Alvarez, R. G. Melko, J. Carrasquilla, M. Franz, and M. H. Amin, Computational supremacy in quantum simulation (2024), arXiv:2403.00910 [quant-ph].

[11] S. Zhou, D. Green, E. D. Dahl, and C. Chamon, *Experimental realization of classical F_2 spin liquids in a programmable quantum device*, Phys. Rev. B **104**, L081107 (2021).

[12] P. Narasimhan, S. Humeniuk, A. Roy, and V. Drouin-Touchette, *Simulating the transverse-field ising model on the kagome lattice using a programmable quantum an-*

nealer, Phys. Rev. B **110**, 054432 (2024).

[13] A. Lopez-Bezanilla, J. Raymond, K. Boothby, J. Carrasquilla, C. Nisoli, and A. D. King, *Kagome qubit ice*, Nature communications **14**, 1105 (2023).

[14] A. Lopez-Bezanilla, A. D. King, C. Nisoli, and A. Saxena, *Quantum fluctuations drive nonmonotonic correlations in a qubit lattice*, Nature Communications **15**, 589 (2024).

[15] P. Kairys, A. D. King, I. Ozfidan, K. Boothby, J. Raymond, A. Banerjee, and T. S. Humble, *Simulating the Shastry-Sutherland Ising Model Using Quantum Annealing*, PRX Quantum **1**, 10.1103/prxquantum.1.020320 (2020).

[16] E. Pelofske, F. Barrows, P. Sathe, and C. Nisoli, Magnetic hysteresis experiments performed on quantum annealers (2025), arXiv:2506.17418 [quant-ph].

[17] F. Barrows, E. Pelofske, P. Sathe, F. Caravelli, and C. Nisoli, Magnetic Memory and Hysteresis from Quantum Transitions: Theory and Experiments on Quantum Annealers (2025), arXiv:2507.18079 [quant-ph].

[18] S. A. Makhlouf, F. T. Parker, and A. E. Berkowitz, *Magnetic hysteresis anomalies in ferritin*, Phys. Rev. B **55**, R14717–R14720 (1997).

[19] C. Gilles, P. Bonville, H. Rakoto, J.-M. Broto, K. Wong, and S. Mann, *Magnetic hysteresis and superantiferromagnetism in ferritin nanoparticles*, Journal of Magnetism and Magnetic Materials **241**, 430–440 (2002).

[20] S. Mijatović, S. Graovac, D. Spasojević, and B. Tadić, *Hysteresis loop shape of field-driven antiferromagnetic-ferromagnetic bilayers in experimental conditions*, Phys. Rev. B **111**, 064304 (2025).

[21] M. J. Grzybowski, C. F. Schippers, O. Gomonay, K. Rubi, M. E. Bal, U. Zeitler, A. Kozioł-Rachwał, M. Szpytma, W. Janus, B. Kurowska, S. Kret, M. Gryglas-Borysiewicz, B. Koopmans, and H. J. M. Swagten, *Antiferromagnetic hysteresis above the spin-flop field*, Phys. Rev. B **107**, L060403 (2023).

[22] A. Paduan-Filho, C. C. Becerra, and F. Palacio, *Hysteresis at the spin-flop transition in the antiferromagnets $k_2fe(cl_{1-x}br_x)_5 \cdot h_2o$*, Phys. Rev. B **43**, 11107–11111 (1991).

[23] L. Opherden, T. Bilitewski, J. Hornung, T. Herrmannsdörfer, A. Samartzis, A. Islam, V. Anand, B. Lake, R. Moessner, and J. Wosnitza, *Inverted hysteresis and negative remanence in a homogeneous antiferromagnet*, Physical Review B **98**, 180403 (2018).

[24] B. K. Chakrabarti and M. Acharyya, *Dynamic transitions and hysteresis*, Reviews of Modern Physics **71**, 847 (1999).

[25] F. Broner, G. H. Goldsztein, and S. H. Strogatz, *Dynamical hysteresis without static hysteresis: scaling laws and asymptotic expansions*, SIAM Journal on Applied Mathematics **57**, 1163–1187 (1997).

[26] R. Moessner and S. L. Sondhi, *Ising models of quantum frustration*, Phys. Rev. B **63**, 224401 (2001).

[27] M. W. Johnson, M. H. Amin, S. Gildert, T. Lanting, F. Hamze, N. Dickson, R. Harris, A. J. Berkley, J. Johansson, P. Bunyk, *et al.*, *Quantum annealing with manufactured spins*, Nature **473**, 194–198 (2011).

[28] T. Lanting, A. Przybysz, A. Smirnov, F. Spedalieri, M. Amin, A. Berkley, R. Harris, F. Altomare,

S. Boixo, P. Bunyk, N. Dickson, C. Enderud, J. Hilton, E. Hoskinson, M. Johnson, E. Ladizinsky, N. Ladizinsky, R. Neufeld, T. Oh, I. Perminov, C. Rich, M. Thom, E. Tolkacheva, S. Uchaikin, A. Wilson, and G. Rose, *Entanglement in a Quantum Annealing Processor*, Physical Review X **4**, 10.1103/physrevx.4.021041 (2014).

[29] P. I. Bunyk, E. M. Hoskinson, M. W. Johnson, E. Tolkacheva, F. Altomare, A. J. Berkley, R. Harris, J. P. Hilton, T. Lanting, A. J. Przybysz, and J. Whittaker, *Architectural Considerations in the Design of a Superconducting Quantum Annealing Processor*, IEEE Transactions on Applied Superconductivity **24**, 1–10 (2014).

[30] N. G. Dickson, M. W. Johnson, M. Amin, R. Harris, F. Altomare, A. J. Berkley, P. Bunyk, J. Cai, E. Chapple, P. Chavez, *et al.*, *Thermally assisted quantum annealing of a 16-qubit problem*, Nature communications **4**, 1903 (2013).

[31] R. Harris, M. W. Johnson, T. Lanting, A. J. Berkley, J. Johansson, P. Bunyk, E. Tolkacheva, E. Ladizinsky, N. Ladizinsky, T. Oh, F. Cioata, I. Perminov, P. Spear, C. Enderud, C. Rich, S. Uchaikin, M. C. Thom, E. M. Chapple, J. Wang, B. Wilson, M. H. S. Amin, N. Dickson, K. Karimi, B. Macready, C. J. S. Truncik, and G. Rose, *Experimental investigation of an eight-qubit unit cell in a superconducting optimization processor*, Phys. Rev. B **82**, 024511 (2010).

[32] M. W. Johnson, P. Bunyk, F. Maibaum, E. Tolkacheva, A. J. Berkley, E. M. Chapple, R. Harris, J. Johansson, T. Lanting, I. Perminov, E. Ladizinsky, T. Oh, and G. Rose, *A scalable control system for a superconducting adiabatic quantum optimization processor*, Superconductor Science and Technology **23**, 065004 (2010).

[33] A. D. King, S. Suzuki, J. Raymond, A. Zucca, T. Lanting, F. Altomare, A. J. Berkley, S. Ejtemaee, E. Hoskinson, S. Huang, *et al.*, *Coherent quantum annealing in a programmable 2,000 qubit ising chain*, Nature Physics **18**, 1324–1328 (2022).

[34] A. D. King, J. Raymond, T. Lanting, R. Harris, A. Zucca, F. Altomare, A. J. Berkley, K. Boothby, S. Ejtemaee, C. Enderud, *et al.*, *Quantum critical dynamics in a 5,000-qubit programmable spin glass*, Nature **617**, 61–66 (2023).

[35] M. H. Amin, *Searching for quantum speedup in quasistatic quantum annealers*, Physical Review A **92**, 10.1103/physreva.92.052323 (2015).

[36] E. Pelofske, G. Hahn, and H. N. Djidjev, *Noise dynamics of quantum annealers: estimating the effective noise using idle qubits*, Quantum Science and Technology **8**, 035005 (2023).

[37] Z. Morrell, M. Vuffray, A. Y. Lokhov, A. Bärtschi, T. Albash, and C. Coffrin, *Signatures of Open and Noisy Quantum Systems in Single-Qubit Quantum Annealing*, Phys. Rev. Appl. **19**, 034053 (2023).

[38] J. Marshall, E. G. Rieffel, and I. Hen, *Thermalization, Freeze-out, and Noise: Deciphering Experimental Quantum Annealers*, Phys. Rev. Appl. **8**, 064025 (2017).

[39] J. Nelson, M. Vuffray, A. Y. Lokhov, and C. Coffrin, Single-Qubit Fidelity Assessment of Quantum Annealing Hardware (2021), arXiv:2104.03335 [quant-ph].

[40] T. Zaborniak and R. de Sousa, *Benchmarking Hamiltonian Noise in the D-Wave Quantum Annealer*, IEEE Transactions on Quantum Engineering **2**, 1–6 (2021).

[41] L. Buffoni and M. Campisi, *Thermodynamics of a quantum annealer*, Quantum Science and Technology **5**, 035013 (2020).

[42] C. Tüysüz, A. Jayakumar, C. Coffrin, M. Vuffray, and A. Y. Lokhov, Learning response functions of analog quantum computers: analysis of neutral-atom and superconducting platforms (2025), arXiv:2503.12520 [quant-ph].

[43] M. Vuffray, C. Coffrin, Y. A. Kharkov, and A. Y. Lokhov, *Programmable Quantum Annealers as Noisy Gibbs Samplers*, PRX Quantum **3**, 020317 (2022).

[44] K. Chern, K. Boothby, J. Raymond, P. Farré, and A. D. King, *Tutorial: calibration refinement in quantum annealing*, Frontiers in Computer Science **5**, 10.3389/fcomp.2023.1238988 (2023).

[45] C. McCreesh, P. Prosser, and J. Trimble, in *International Conference on Graph Transformation* (Springer, 2020) pp. 316–324.

[46] J. Cai, W. G. Macready, and A. Roy, A practical heuristic for finding graph minors (2014), arXiv:1406.2741 [quant-ph].

[47] J. Marshall, A. Di Gioacchino, and E. G. Rieffel, *Perils of embedding for sampling problems*, Phys. Rev. Res. **2**, 023020 (2020).

[48] N. Dattani, S. Szalay, and N. Chancellor, Pegasus: The second connectivity graph for large-scale quantum annealing hardware (2019), arXiv:1901.07636 [quant-ph].

[49] K. Boothby, P. Bunyk, J. Raymond, and A. Roy, Next-Generation Topology of D-Wave Quantum Processors (2020), arXiv:2003.00133 [quant-ph].

[50] K. Boothby, A. D. King, and J. Raymond, Zephyr topology of d-wave quantum processors (2021).

[51] A. D. King, J. Raymond, T. Lanting, R. Harris, A. Zucca, F. Altomare, A. J. Berkley, K. Boothby, S. Ejtemaee, C. Enderud, E. Hoskinson, S. Huang, E. Ladizinsky, A. J. R. MacDonald, G. Marsden, R. Molavi, T. Oh, G. Poulin-Lamarre, M. Reis, C. Rich, Y. Sato, N. Tsai, M. Volkmann, J. D. Whittaker, J. Yao, A. W. Sandvik, and M. H. Amin, *Quantum critical dynamics in a 5,000-qubit programmable spin glass*, Nature **617**, 61–66 (2023).

[52] A. Ali, H. Xu, W. Bernoudy, A. Nocera, A. D. King, and A. Banerjee, *Quantum quench dynamics of geometrically frustrated Ising models*, Nature Communications **15**, 10756 (2024).

[53] P. Sathe, A. D. King, S. M. Mniszewski, C. Coffrin, C. Nisoli, and F. Caravelli, Classical Criticality via Quantum Annealing (2025), arXiv:2505.13625 [cond-mat.stat-mech].

[54] E. Pelofske, G. Hahn, and H. N. Djidjev, in *Proceedings of the 18th ACM International Conference on Computing Frontiers*, CF '21 (ACM, 2021) p. 133–139.

[55] K. Nishimura, H. Nishimori, and H. G. Katzgraber, *Griffiths-McCoy singularity on the diluted Chimera graph: Monte Carlo simulations and experiments on quantum hardware*, Phys. Rev. A **102**, 042403 (2020).

[56] S. K. Lam, A. Pitrou, and S. Seibert, in *Proceedings of the Second Workshop on the LLVM Compiler Infrastructure in HPC*, LLVM '15 (Association for Computing Machinery, New York, NY, USA, 2015).

[57] C. R. Harris, K. J. Millman, S. J. van der Walt, R. Gommers, P. Virtanen, D. Cournapeau, E. Wieser, J. Taylor, S. Berg, N. J. Smith, R. Kern, M. Picus, S. Hoyer, M. H. van Kerkwijk, M. Brett, A. Haldane, J. F. del Río, M. Wiebe, P. Peterson, P. Gérard-Marchant, K. Sheppard, T. Reddy, W. Weckesser, H. Abbasi, C. Gohlke, and T. E. Oliphant, *Array programming with NumPy*, Nature **585**, 357–362 (2020).

[58] W. Jiang, V. cheong Lo, B.-D. Bai, and J. Yang, *Magnetic hysteresis loops in molecular-based magnetic materials afeiifeiii(c2o4)3*, Physica A: Statistical Mechanics and its Applications **389**, 2227–2233 (2010).

[59] Y. LeCun, L. Bottou, Y. Bengio, and P. Haffner, *Gradient-based learning applied to document recognition*, Proceedings of the IEEE **86**, 2278–2324 (2002).

[60] D. E. Rumelhart, G. E. Hinton, and R. J. Williams, *Learning representations by back-propagating errors*, nature **323**, 533–536 (1986).

[61] R. Harris, T. Lanting, A. J. Berkley, J. Johansson, M. W. Johnson, P. Bunyk, E. Ladizinsky, N. Ladizinsky, T. Oh, and S. Han, *Compound josephson-junction coupler for flux qubits with minimal crosstalk*, Phys. Rev. B **80**, 052506 (2009).